Supplement of Solid Earth, 17, 665–687, 2026
https://doi.org/10.5194/se-17-665-2026-supplement

Solid Earth Open Access EGU

Supplement of

First tomographic imaging of mid-crustal doubling at the Abruzzi outer thrust front, central-southern Italy

Rita de Nardis et al.

Correspondence to: Rita de Nardis (rita.denardis@unich.it) and Donato Talone (donato.talone@unich.it)

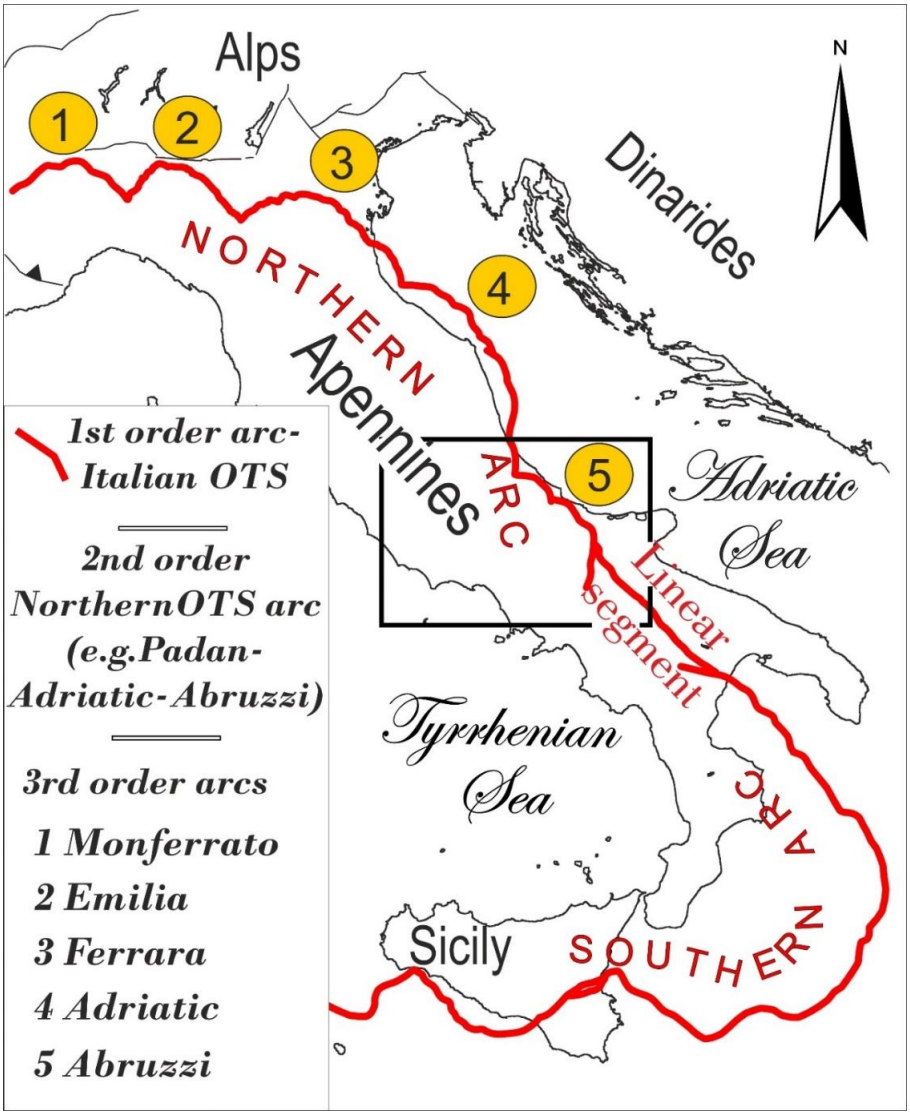

Figure S1. The Italian Outer Thrust System and its second and third-order arcs.

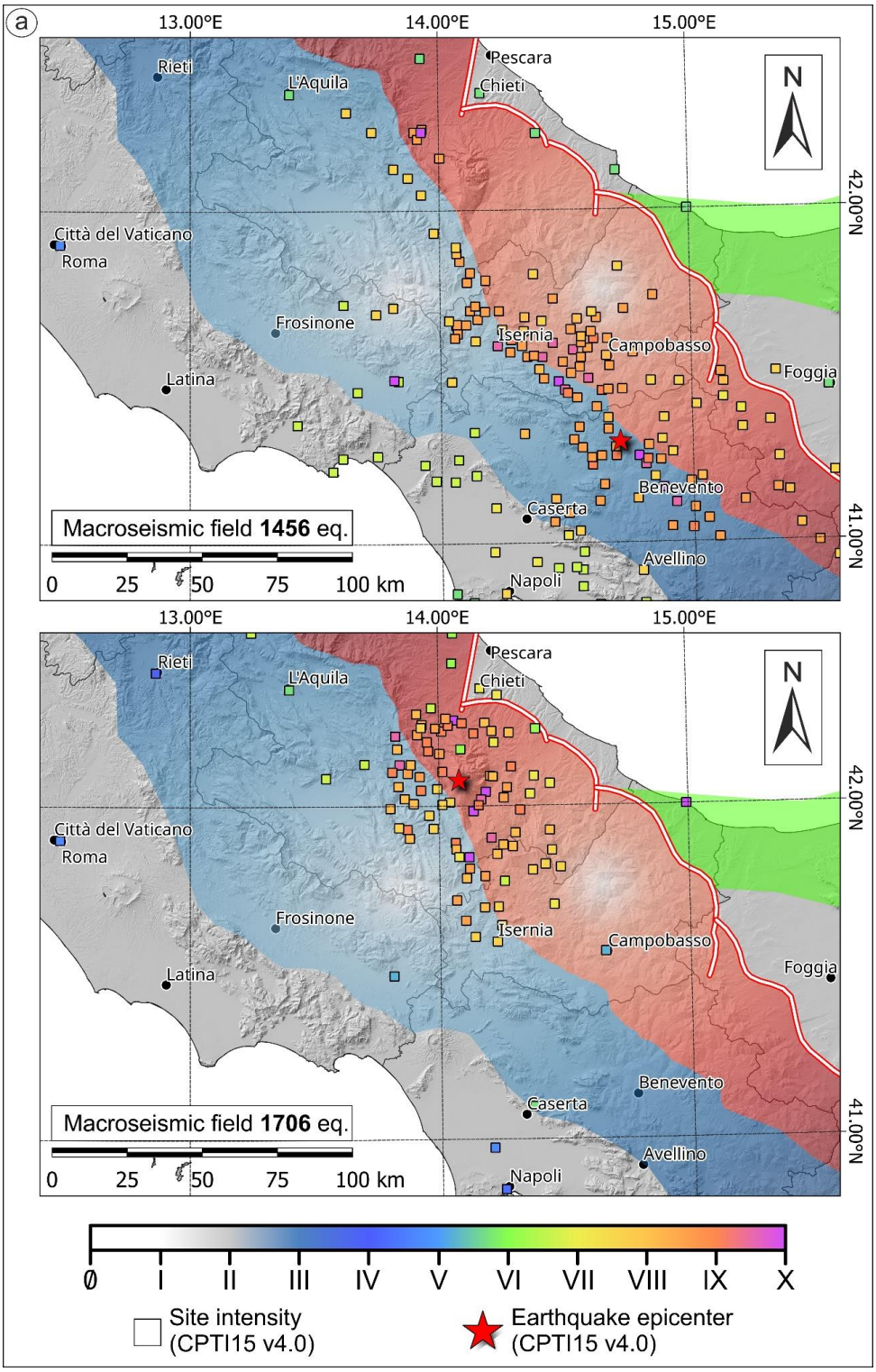
a
13.00°E
14.00°E
15.00°E
42.00°N
41.00°N
N
Rieti
L'Aquila
Pescara
Chieti
Città del Vaticano
Roma
Frosinone
Isernia
Campobasso
Foggia
Latina
Benevento
Caserta
Avellino
Napoli
Macroseismic field 1456 eq.
0 25 50 75 100 km
Macroseismic field 1706 eq.
Ø I II III IV V VI VII VIII IX X
Site intensity (CPTI15 v4.0)
Earthquake epicenter (CPTI15 v4.0)

CONTINUED

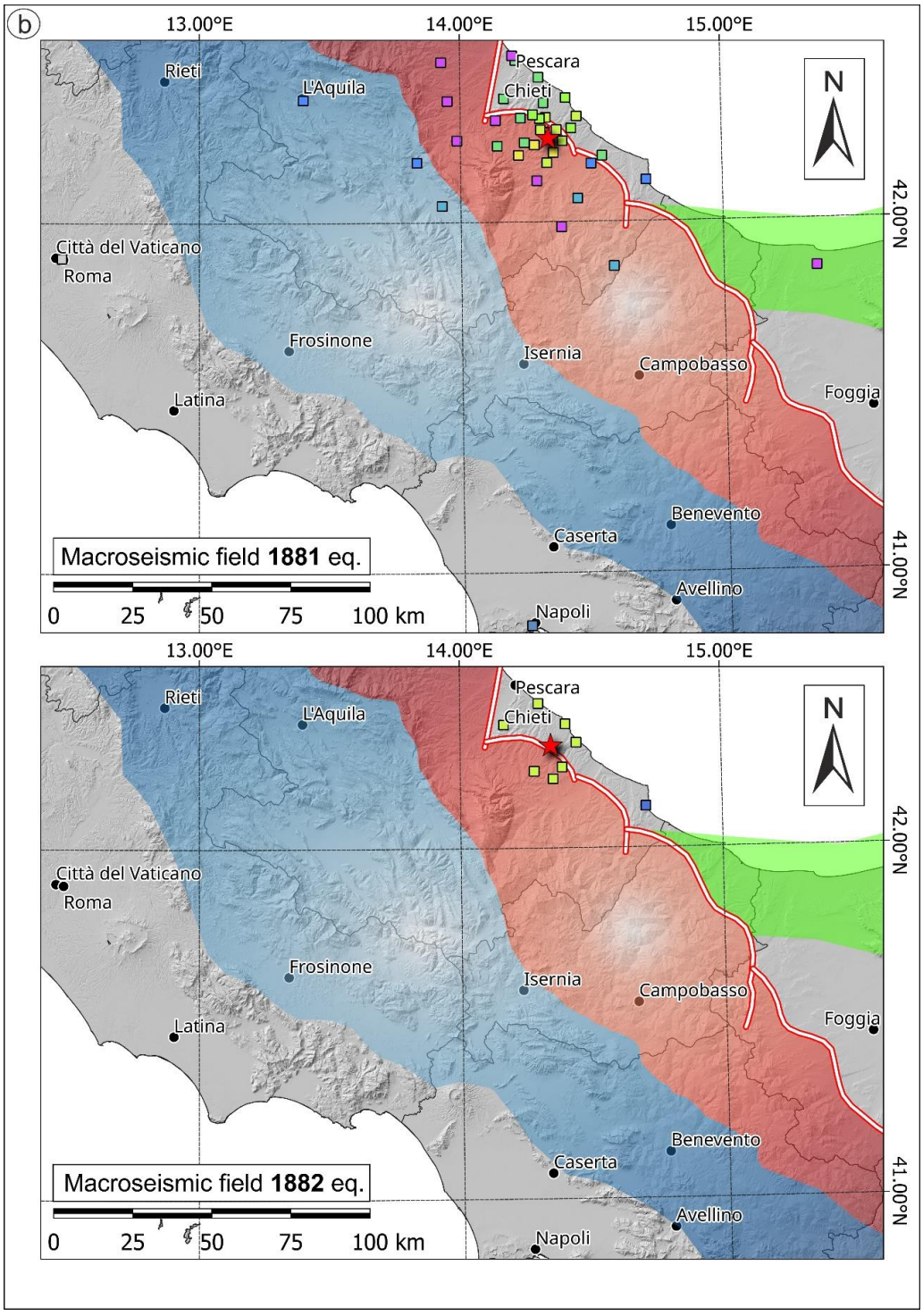
b
13.00°E
14.00°E
15.00°E
42.00°N
41.00°N
Rieti
L'Aquila
Pescara
Chieti
N
Città del Vaticano
Roma
Frosinone
Isernia
Campobasso
Foggia
Latina
Benevento
Caserta
Avellino
Napoli
Macroseismic field 1881 eq.
0 25 50 75 100 km
13.00°E
14.00°E
15.00°E
42.00°N
41.00°N
Rieti
L'Aquila
Pescara
Chieti
N
Città del Vaticano
Roma
Frosinone
Isernia
Campobasso
Foggia
Latina
Benevento
Caserta
Avellino
Napoli
Macroseismic field 1882 eq.
0 25 50 75 100 km

CONTINUED

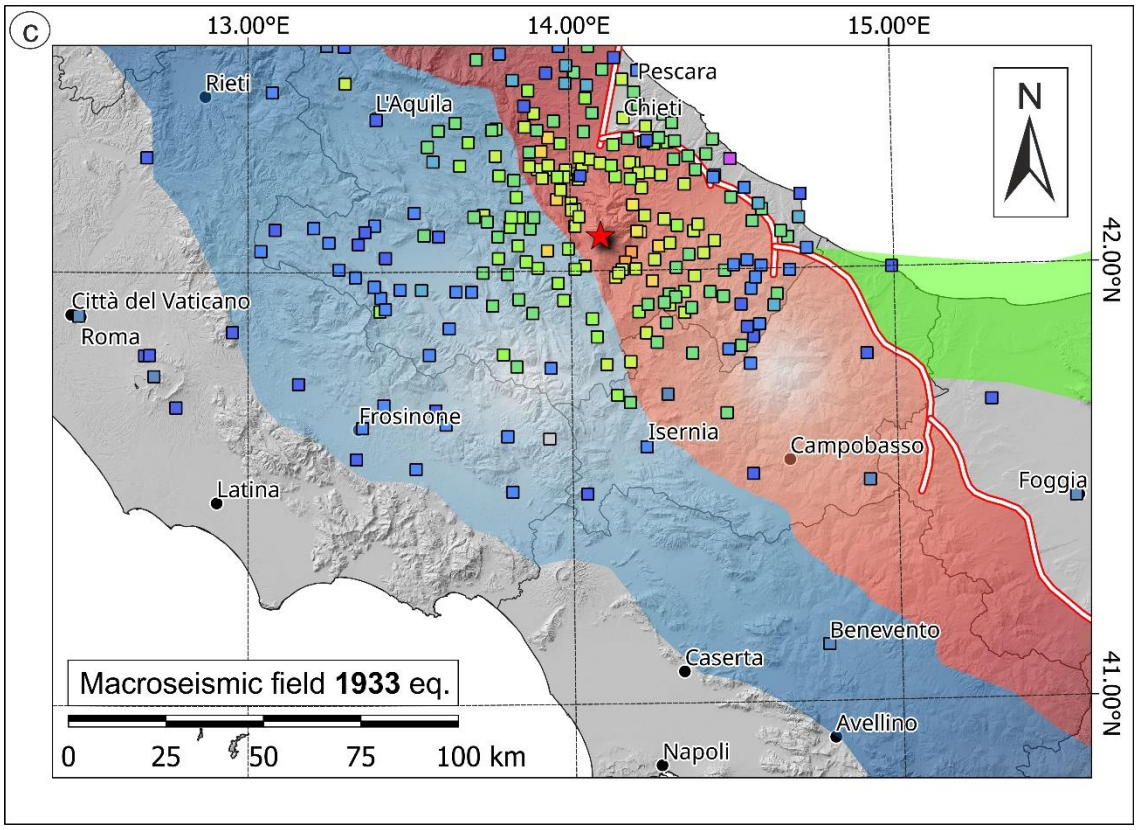

Figure S2. Macroseismic fields of the most significant historical earthquakes occurred in the study area as reported in CPTI15 (Rovida et al., 2020, 2022). a) 1456 (Io=XI, Mw=7.2) and 1706 (Io=X-XI, Mw=6.8). b) 1881 (Io=VII-VIII, Mw=5.4) and 1882 (Io=VII, Mw=5.3). c) 1933 (Io=IX, Mw=5.9). The legend is common and shown in the first panel.

15

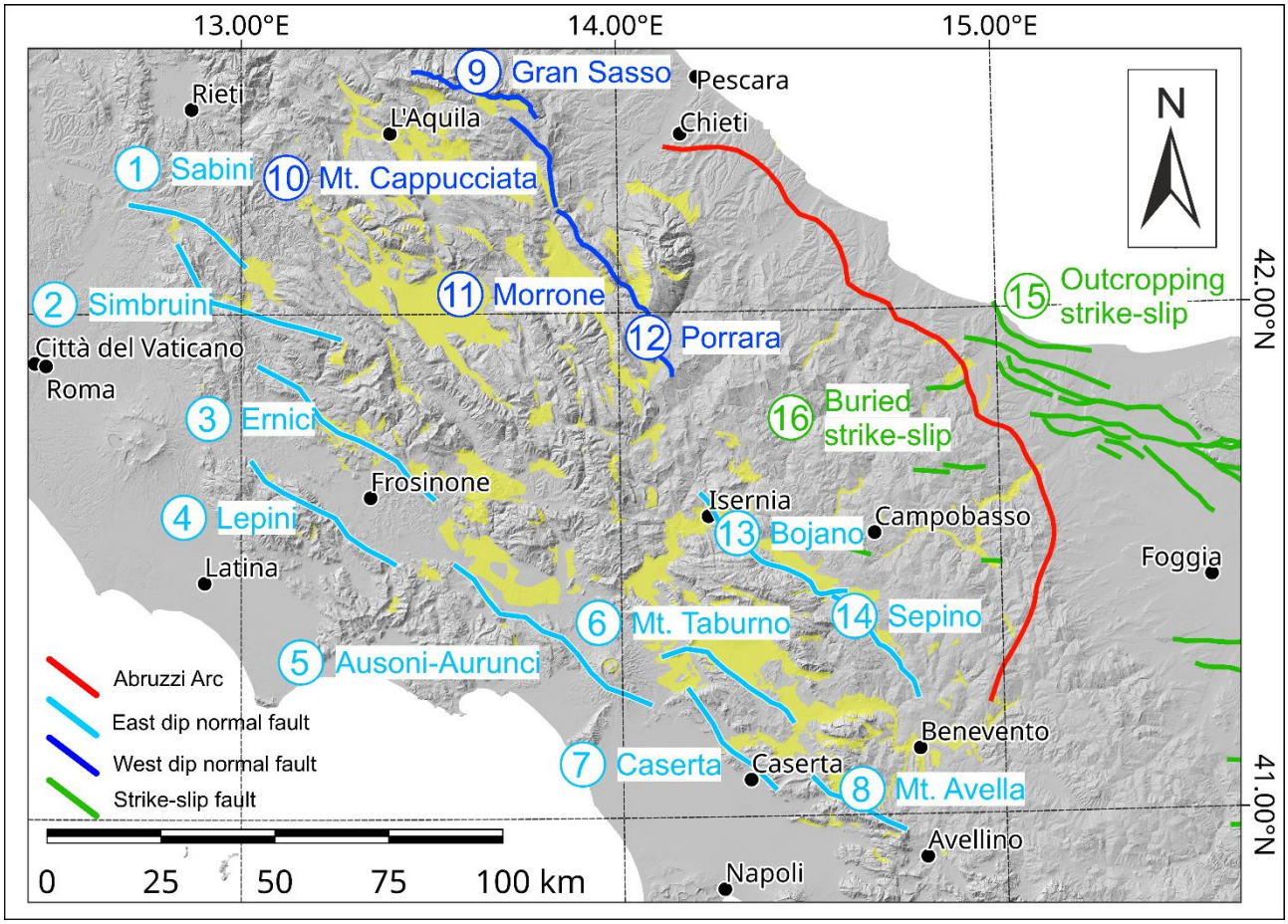

Figure S3. Schematic fault pattern described in the text (Sect. 2). Yellow polygons are quaternary deposits highlighting the position of intramountain basins.

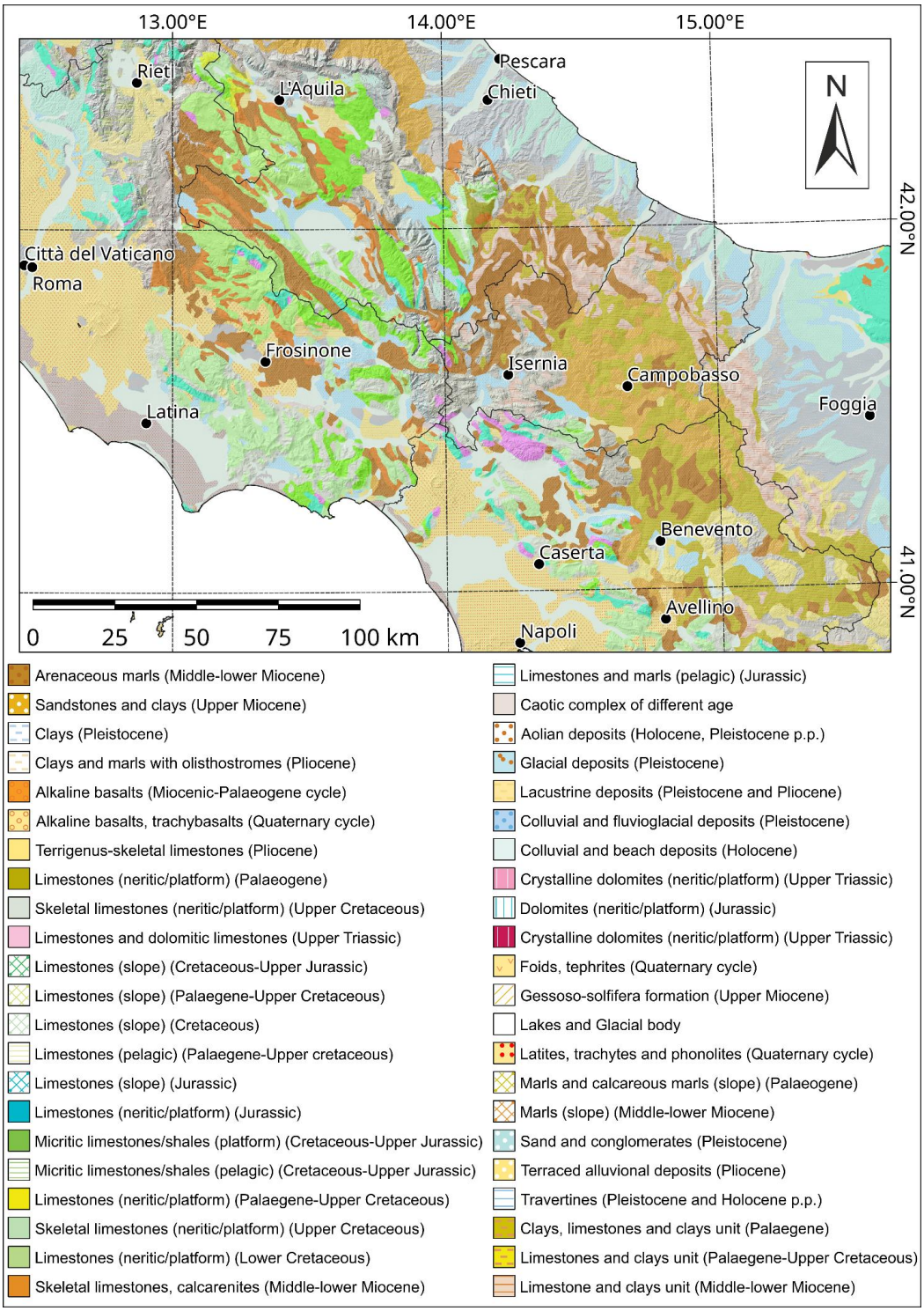

20 **Figure S4. Geological map of central-southern Italy as reported in the Geological and Lithological Units of Italy map at the scale of 1:500,000 (http://portalesgi.isprambiente.it/it/lista-servizi-wms/Geological%20Maps).**

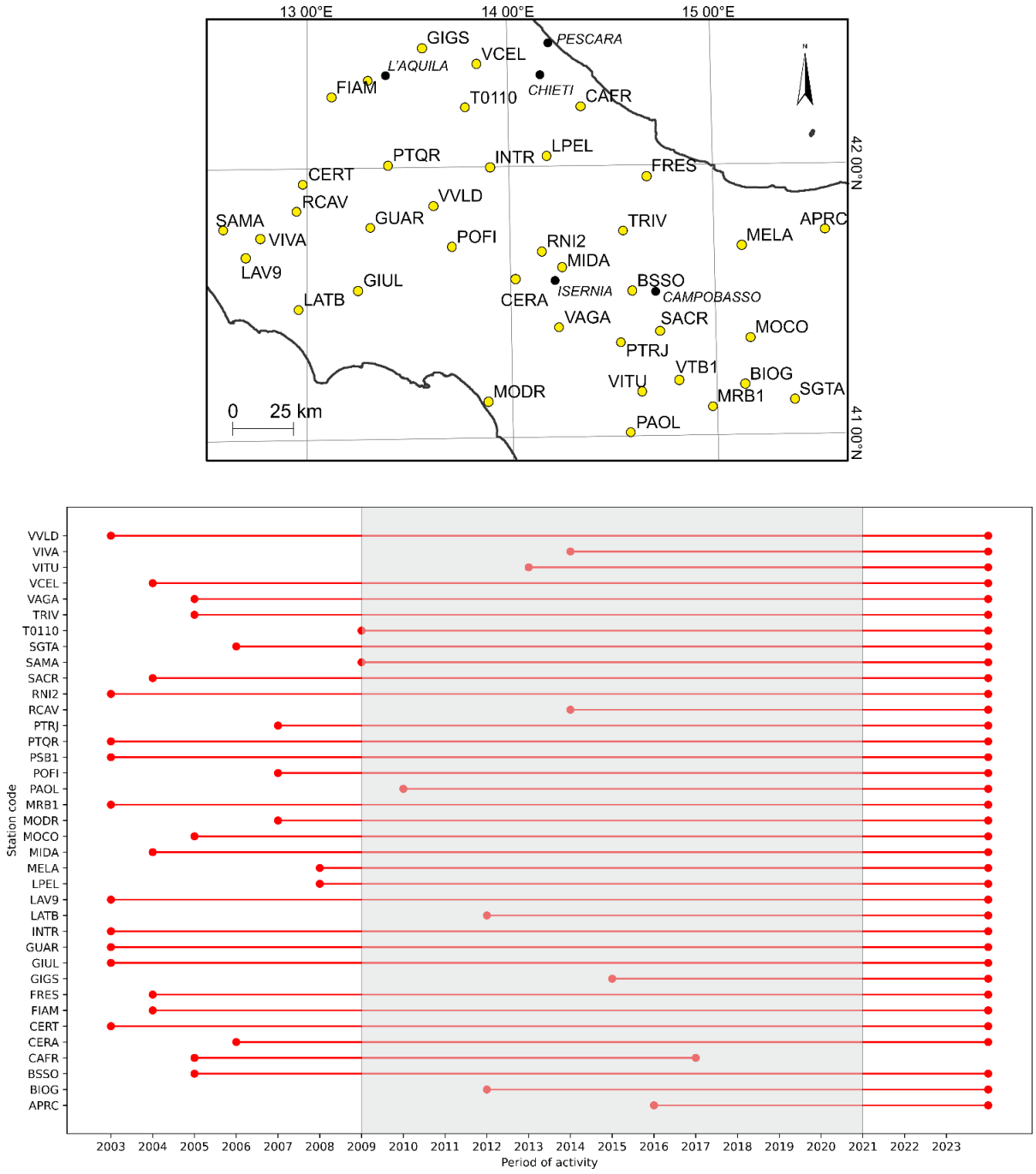

Figure S5. Map (upper panel) and activity time (lower panel) of the seismic stations used for travel time seismic tomography. The grey patch represents the period considered in this study.

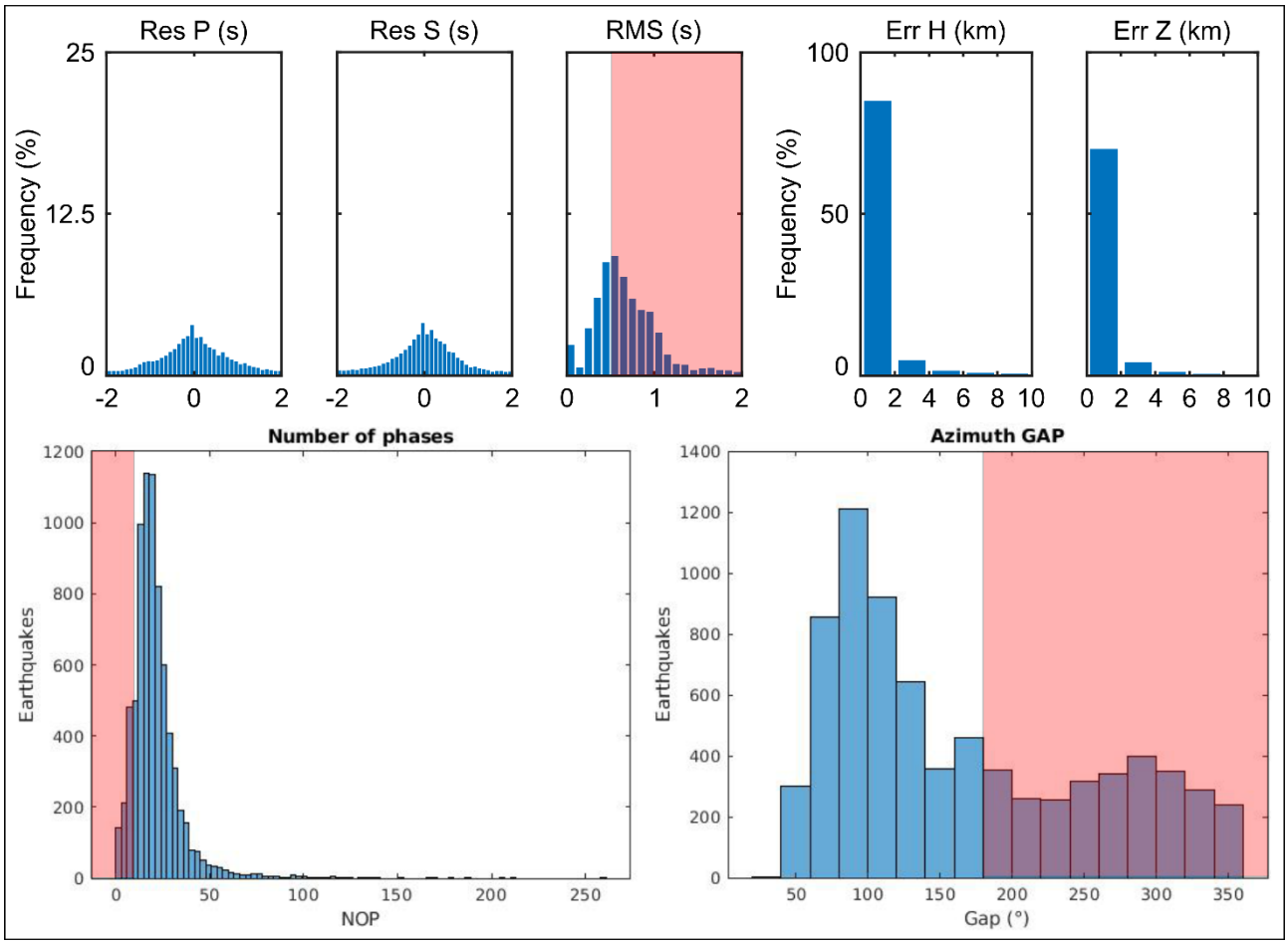

Figure S6. General characteristics of initial and final earthquake location datasets used for seismic tomography. Upper panel: statistical parameters of the preliminary earthquake location performed using the 1D model from (Trionfera et al., 2019). Bottom left side: total number of phases (NOP) histogram recognized for each earthquake at the different stations (sum of P and S for all the stations triggered). Bottom right side: azimuthal gap for the earthquakes in the catalog. Red patches represent the discarded earthquakes after filtering the hypocentral solutions for RMS ≤ 0.5 s, number of phases ≥ 10, and azimuthal gap ≤ 180°.

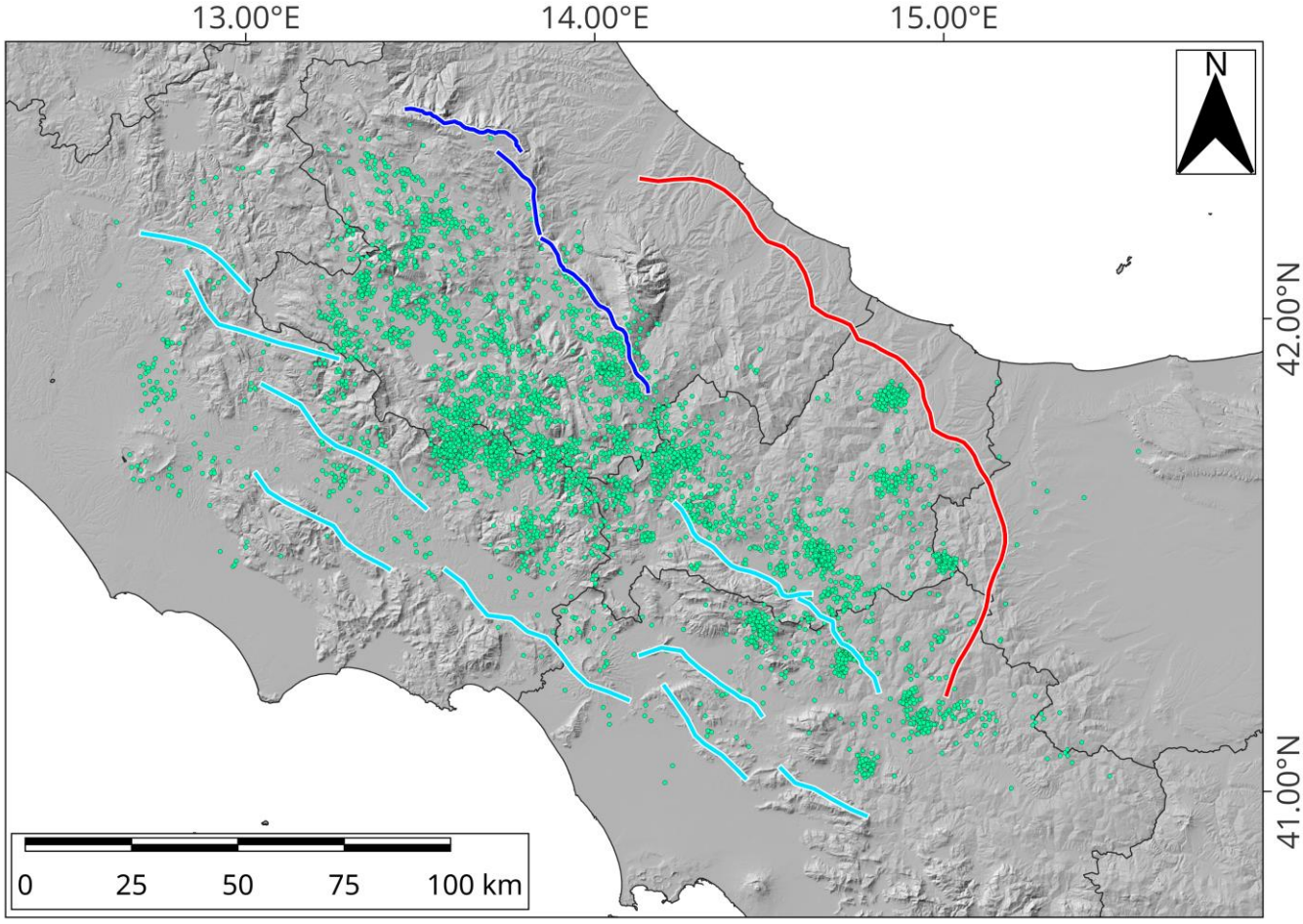

Figure S7. Map of the seismicity catalogue used for the tomography process. Green points are the earthquakes; red line is the outer thrust front; blue lines represent the western east-dipping and the eastern west-dipping boundary of the extensional domain.

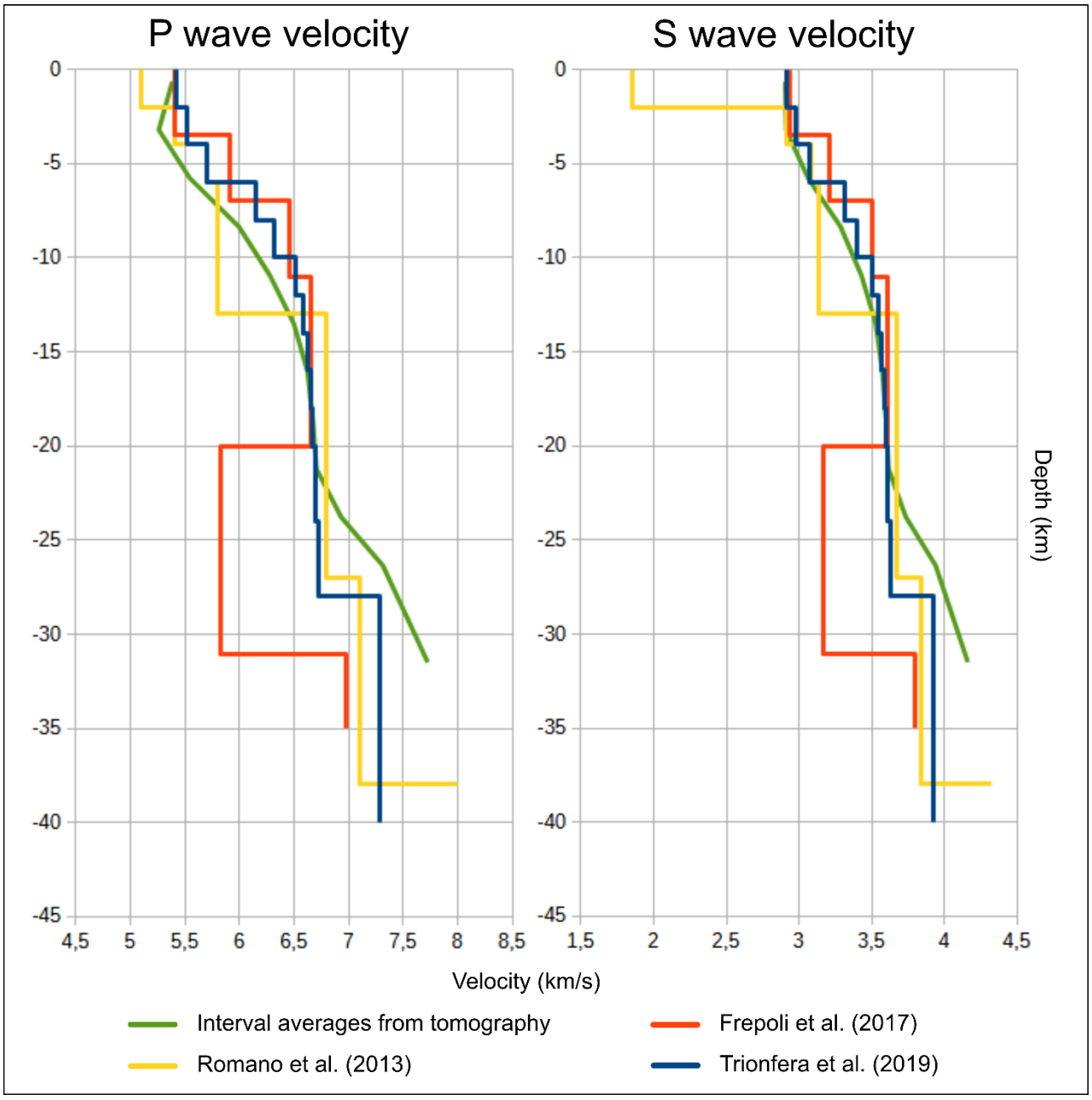

Figure S8. Comparison of the velocity models. Graphical comparison of 1D velocity models (Frepoli et al., 2017; Romano et al., 2013; Trionfera et al., 2019) used in this study as input for the tomographic process. To express the 3D model in a one-dimensional form, we considered the mean of each depth layer in the grid. The velocity models have also been used for re-locating the earthquakes before performing the travel time tomography.

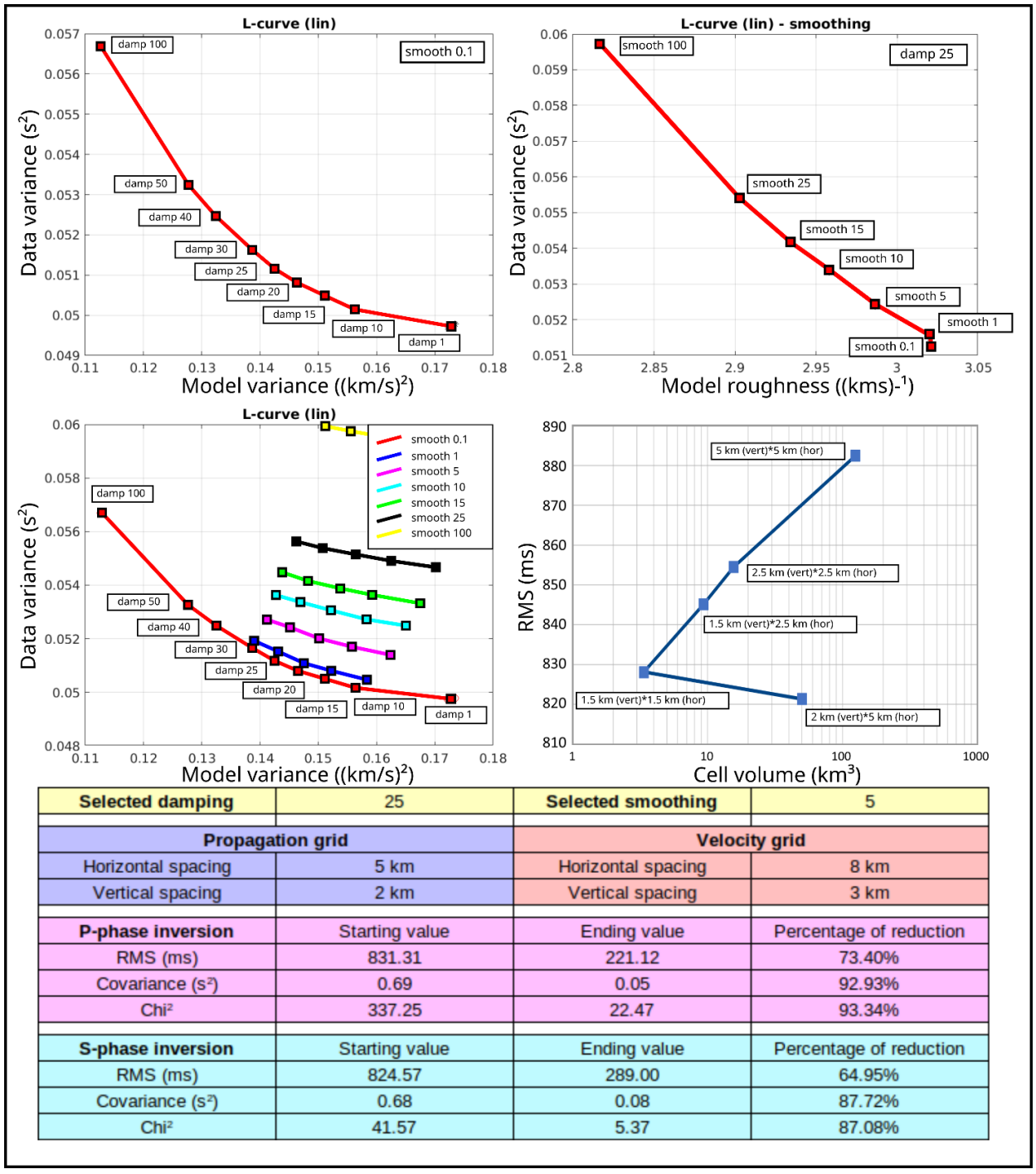

Selected damping	25	Selected smoothing	5
Propagation grid		**Velocity grid**	
Horizontal spacing	5 km	Horizontal spacing	8 km
Vertical spacing	2 km	Vertical spacing	3 km
P-phase inversion	Starting value	Ending value	Percentage of reduction
RMS (ms)	831.31	221.12	73.40%
Covariance (s²)	0.69	0.05	92.93%
Chi²	337.25	22.47	93.34%
S-phase inversion	Starting value	Ending value	Percentage of reduction
RMS (ms)	824.57	289.00	64.95%
Covariance (s²)	0.68	0.08	87.72%
Chi²	41.57	5.37	87.08%

40 **Figure S9. Inversion parameters for the seismic tomographic process. The trade-off curves have been used to select the best values for damping and smoothing parameters. Top-left: data variance vs model variance, having a fixed smoothing and variable damping; top-right: data variance vs model roughness, having a fixed damping and a variable smoothing; bottom-left: data variance vs model variance, having variable smoothing and damping; bottom-right: influence of grid spacing on the starting RMS value. The table summarizes the inversion parameters, grid dimension, and misfit reduction for P and S tomographic models.**

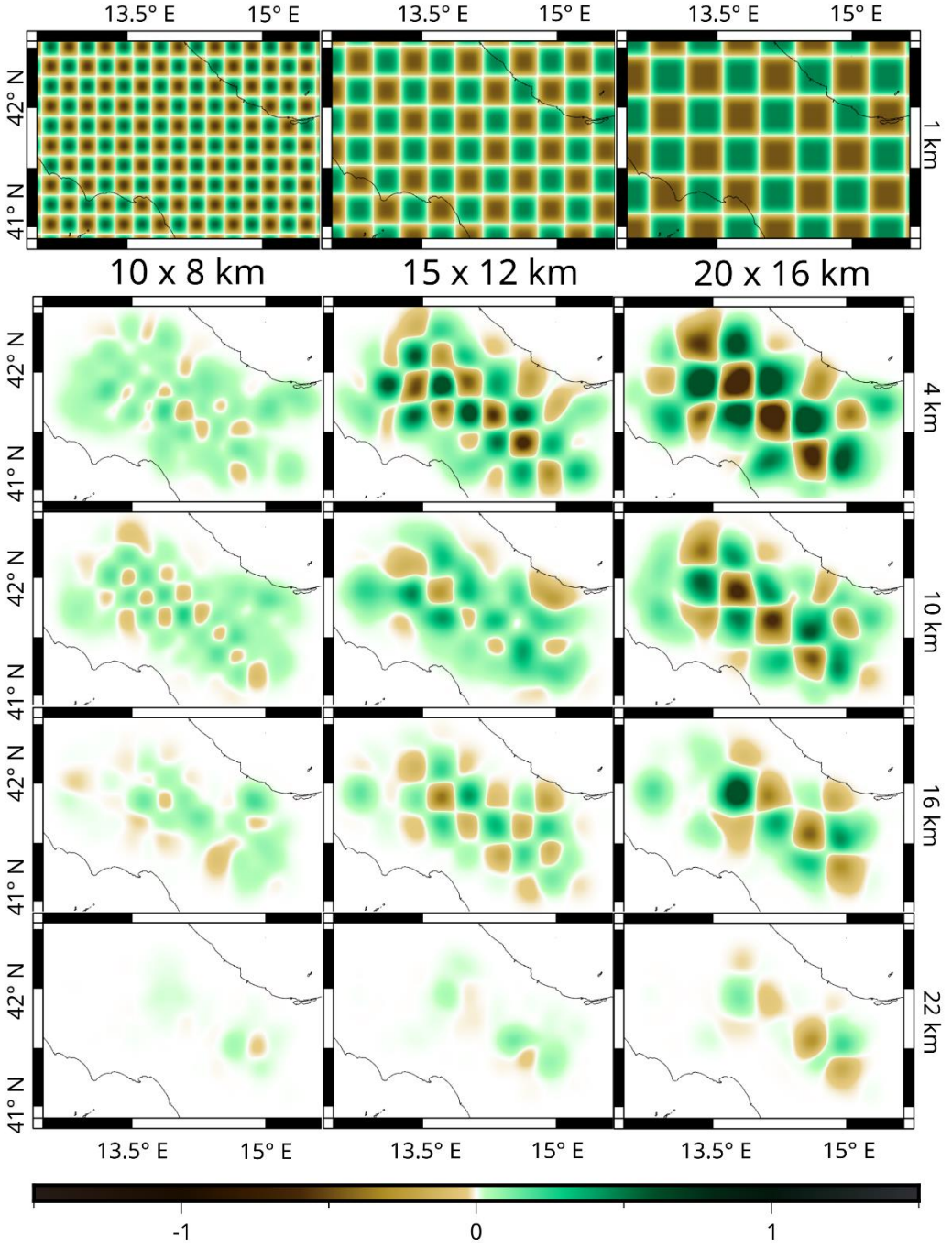

Figure S10. P-model checkerboard tests are represented on a horizontal section by cutting the model each 6 km (on the right edge is reported the depth). Each column shows a different dimension of the checkerboard cells: in the first one, the cells are 10 km horizontal and 8 km vertical; in the second one, the checkerboard is 15 km horizontal and 12 km vertical; in the third one, the cells are 20 km horizontal and 16 km vertical. Seismic velocity is represented as a variation in km/s from uniform fixed values of 6.4 km/s (median of the 1D starting velocity model).

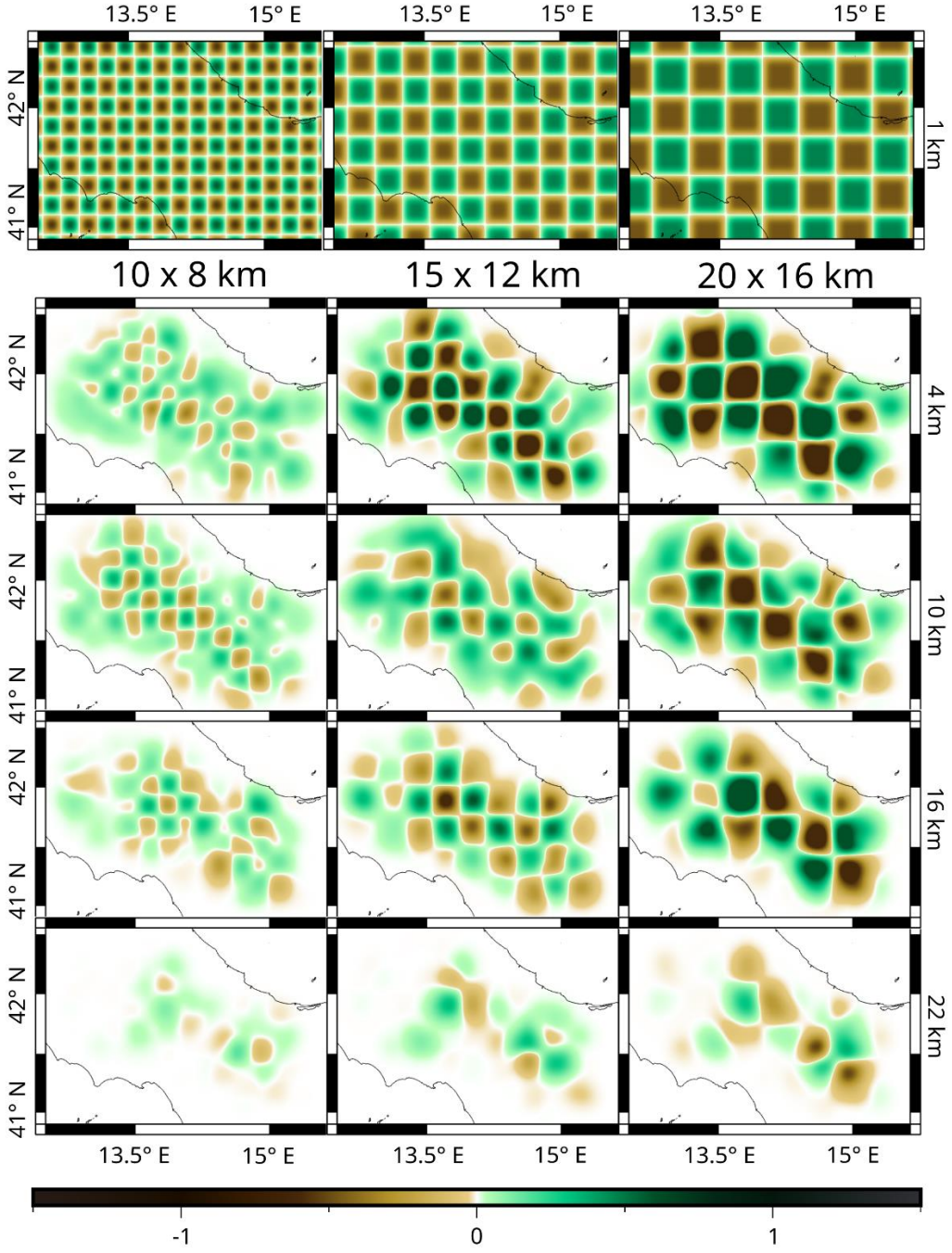

Figure S11. S-model checkerboard tests are represented on a horizontal section by cutting the model each 6 km (on the right edge is reported the depth). Each column shows a different dimension of the checkerboard cells: in the first one, the cells are 10 km horizontal and 8 km vertical; in the second one, the checkerboard is 15 km horizontal and 12 km vertical; in the third one, the cells are 20 km horizontal and 16 km vertical. Seismic velocity is represented as a variation in km/s from uniform fixed values of 3.4 km/s (median of the 1D starting velocity model).

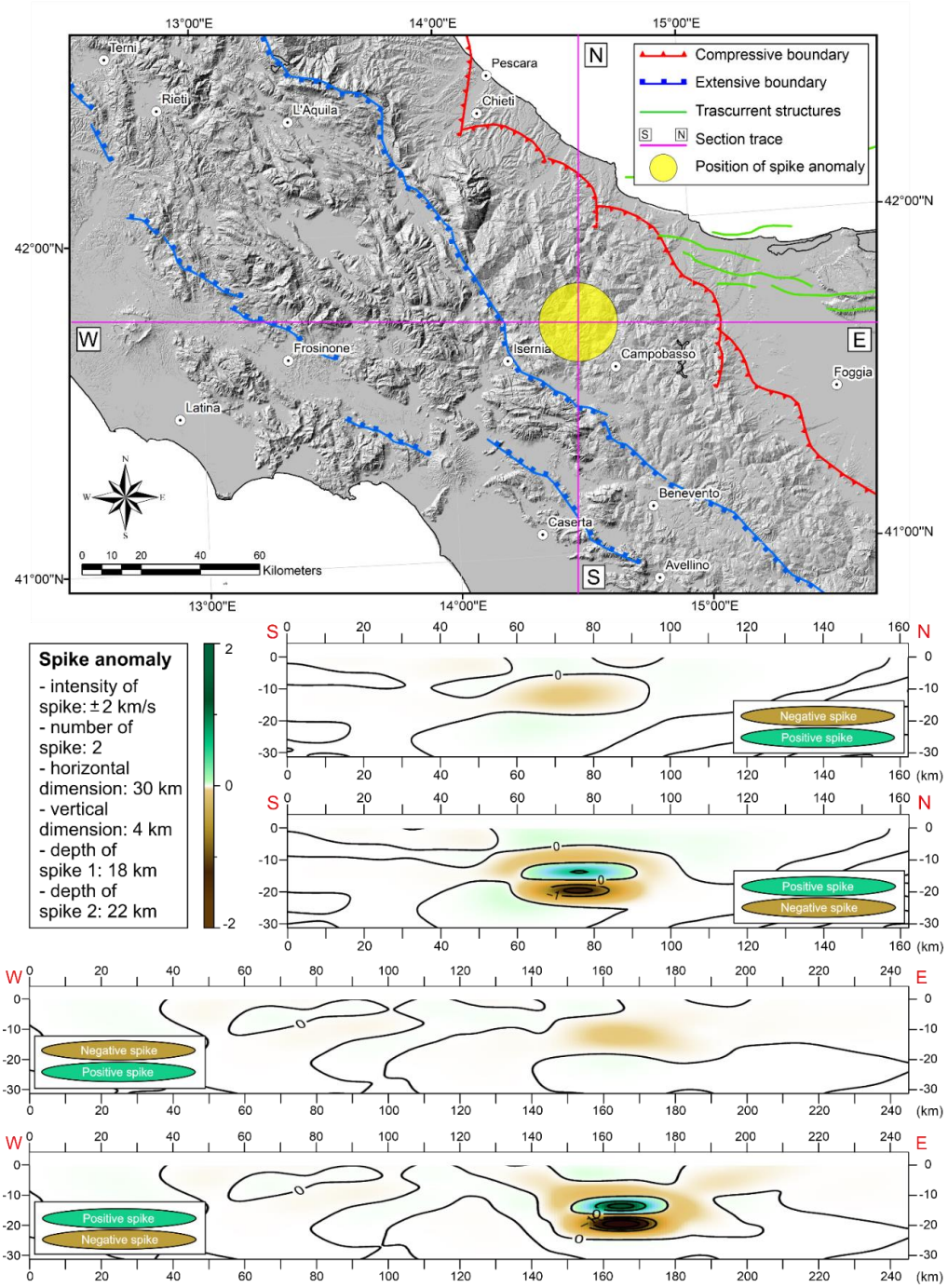

Figure S12. Spike test to verify the reliability of velocity inversion at depth. The location map above shows the position of synthetic spikes. The centres of the two anomalies (positive and negative) are located at depths of 18 km and 22 km, respectively; they are 30 km wide in the horizontal direction, and 4 km thick in the vertical direction, with a value of +2 km/s and -2 km/s. As shown in the location map, vertical sections cross the entire model in S-N and W-E directions. In both cases, the first section crosses the reverse spike output model (negative over positive velocity anomaly), while the second one crosses the normal spike output model (positive over negative velocity anomaly).

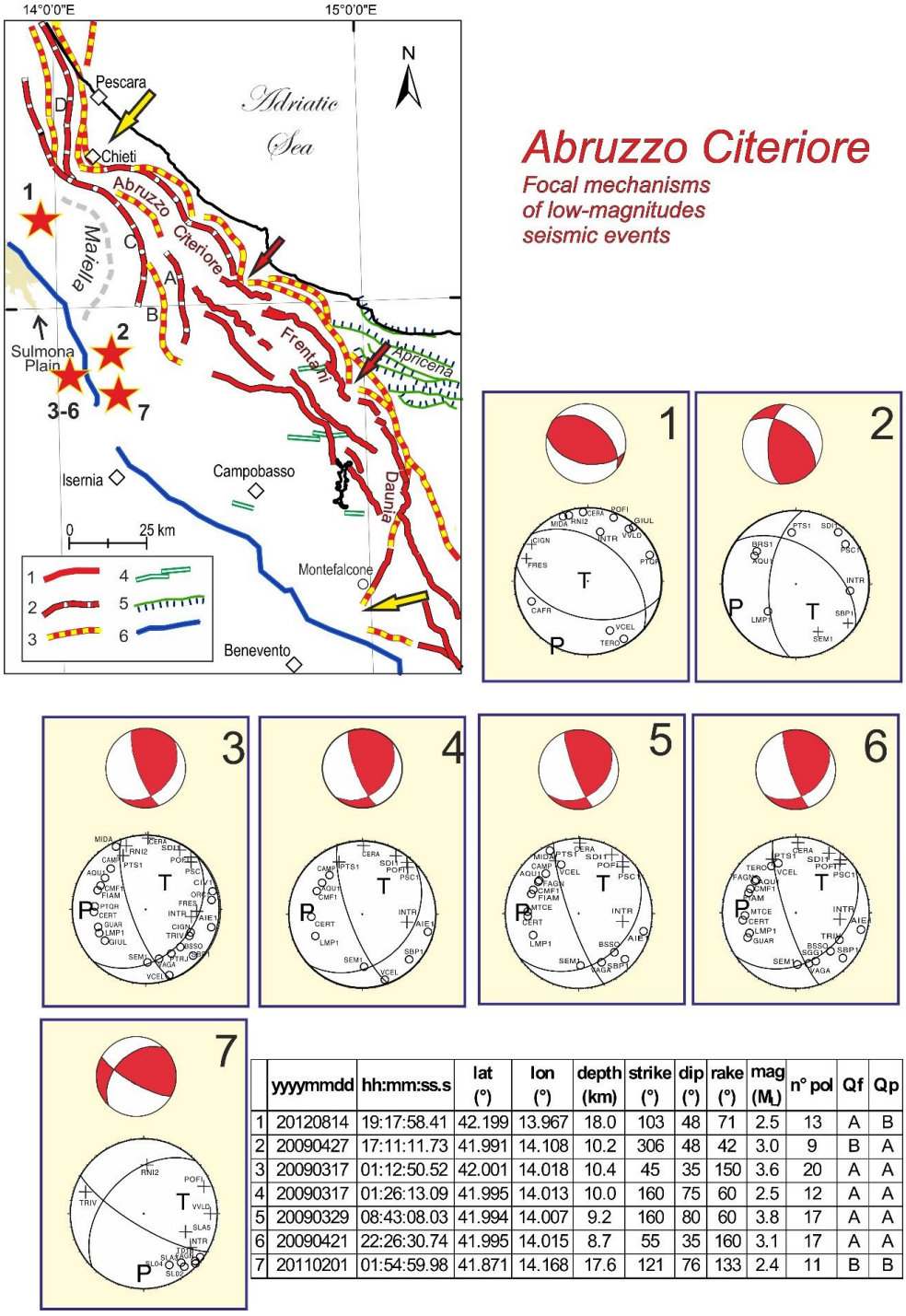

	yyyymmdd	hh:mm:ss.s	lat (°)	lon (°)	depth (km)	strike (°)	dip (°)	rake (°)	mag (M_L)	n° pol	Qf	Qp
1	20120814	19:17:58.41	42.199	13.967	18.0	103	48	71	2.5	13	A	B
2	20090427	17:11:11.73	41.991	14.108	10.2	306	48	42	3.0	9	B	A
3	20090317	01:12:50.52	42.001	14.018	10.4	45	35	150	3.6	20	A	A
4	20090317	01:26:13.09	41.995	14.013	10.0	160	75	60	2.5	12	A	A
5	20090329	08:43:08.03	41.994	14.007	9.2	160	80	60	3.8	17	A	A
6	20090421	22:26:30.74	41.995	14.015	8.7	55	35	160	3.1	17	A	A
7	20110201	01:54:59.98	41.871	14.168	17.6	121	76	133	2.4	11	B	B

65 **Figure S13. Focal mechanism solutions computed in this study using data from the National Seismic Network, temporary network, and Abruzzo network (Romano et al., 2013). Red stars indicate the position of the events for which the focal mechanism has been performed. Structural keys 1-5 in the map are the same as in Figure 3 of the main text; key 6 are principal normal fault alignments.**

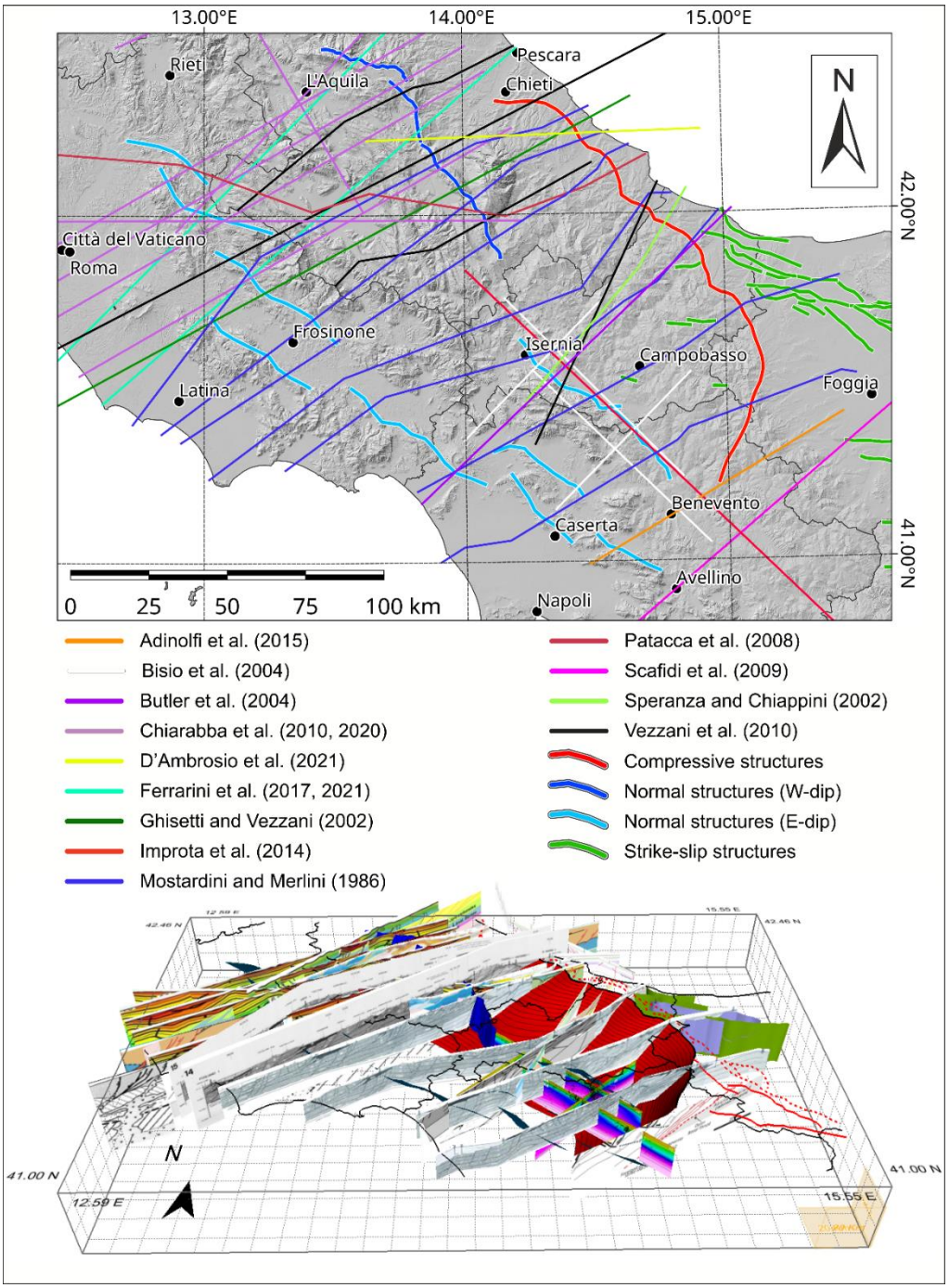

Figure S14. Geological and geophysical sections collected for building the 3D model of the study area (Adinolfi et al., 2015; Bisio et al., 2004; Butler et al., 2004; Chiarabba et al., 2010, 2020; D'Ambrosio et al., 2021; Ferrarini et al., 2017, 2021; Ghisetti and Vezzani, 2002; Improta et al., 2014; Mostardini and Merlini, 1986; Patacca et al., 2008; Scafidi et al., 2009; Speranza and Chiappini, 2002; Vezzani et al., 2010). Other bibliographic citations in the main text refer to structural maps without associated sections.

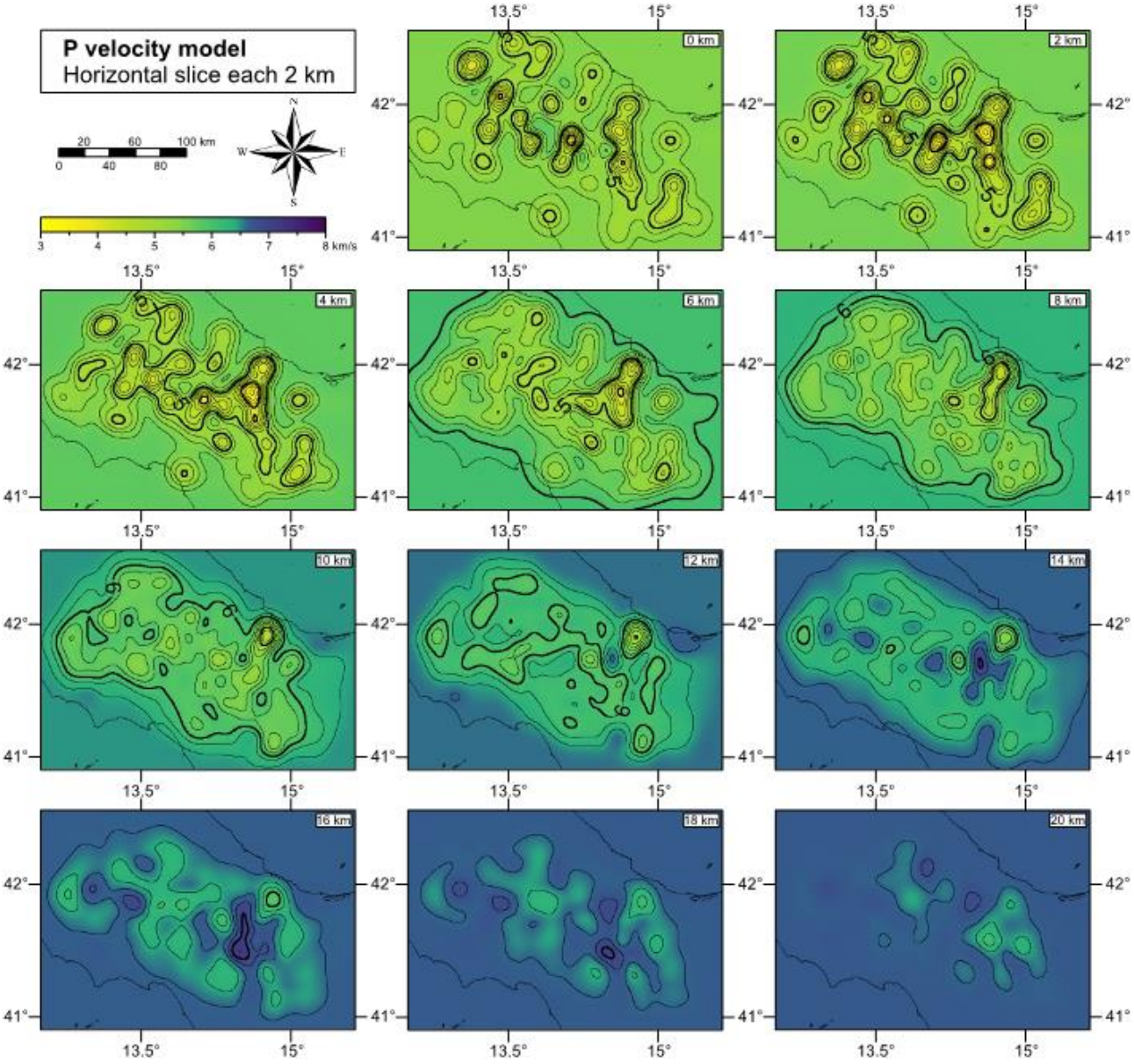

Figure S15. Horizontal slice of the P-velocity tomographic model. Slices represents the velocity model at intervals of 2 km in depth as indicated in the upper-right corner of each image. Main contour lines have a step of 1 km/s.

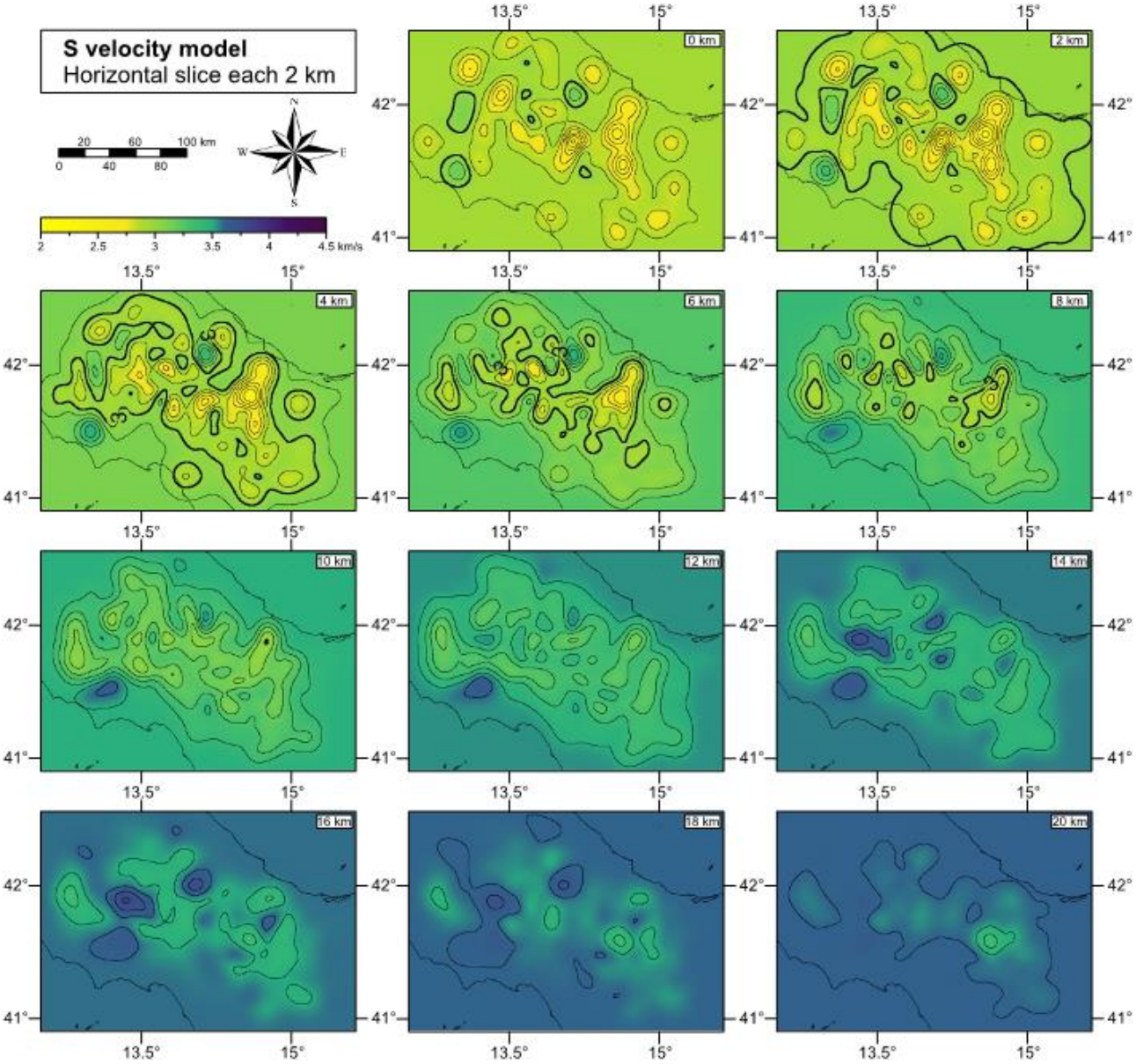

Figure S16. Horizontal slice of the S-velocity tomographic model. Slices represents the velocity model at intervals of 2 km in depth as indicated in the upper-right corner of each image. Main contour lines have a step of 1 km/s.

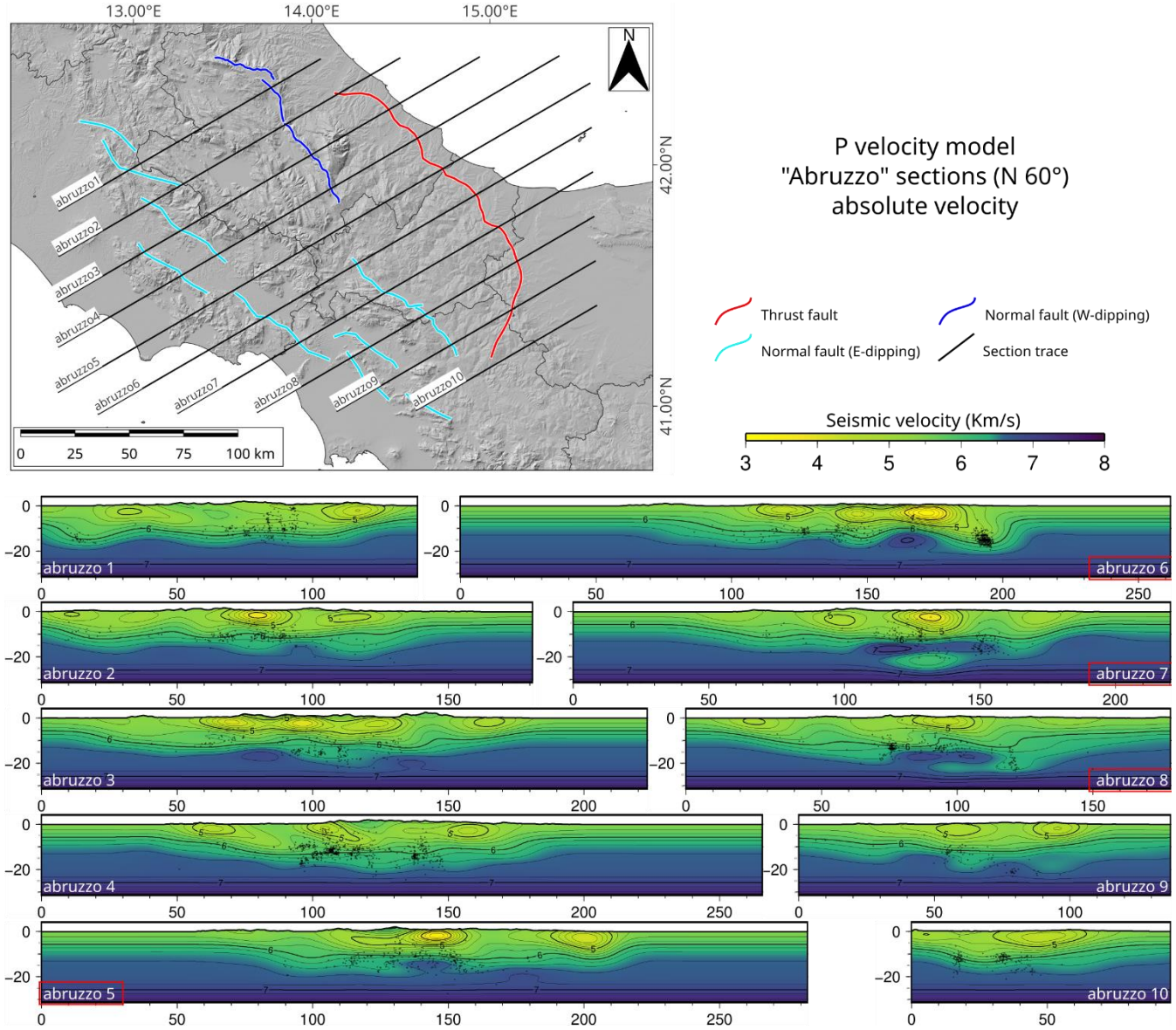

80 **Figure S17. Vertical slices of the P tomographic model. Ten vertical cross-sections (abruzzo1-abruzzo10) spaced 9 km apart and oriented N60°E. The main contour lines are spaced at 1 km/s intervals, and the values are represented as absolute velocity. Red rectangle highlight the sections showing the velocity inversion.**

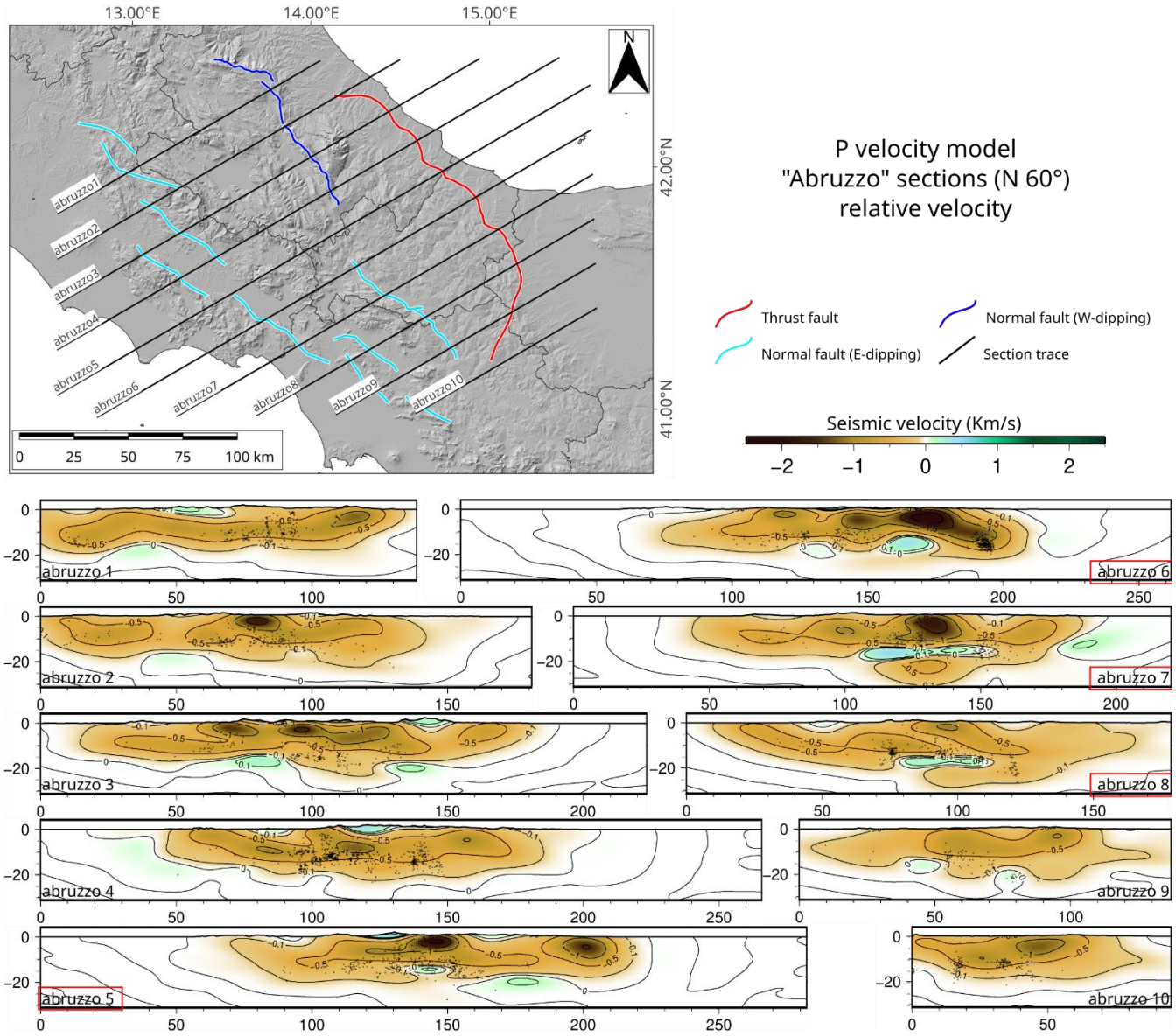

Figure S18. Vertical slices of the P tomographic model. Ten vertical cross-sections (abruzzo1-abruzzo10) spaced 9 km apart and oriented N60°E. The main contour lines are spaced at 1 km/s intervals, and the values are represented as relative velocity. Red rectangle highlight the sections showing the velocity inversion.

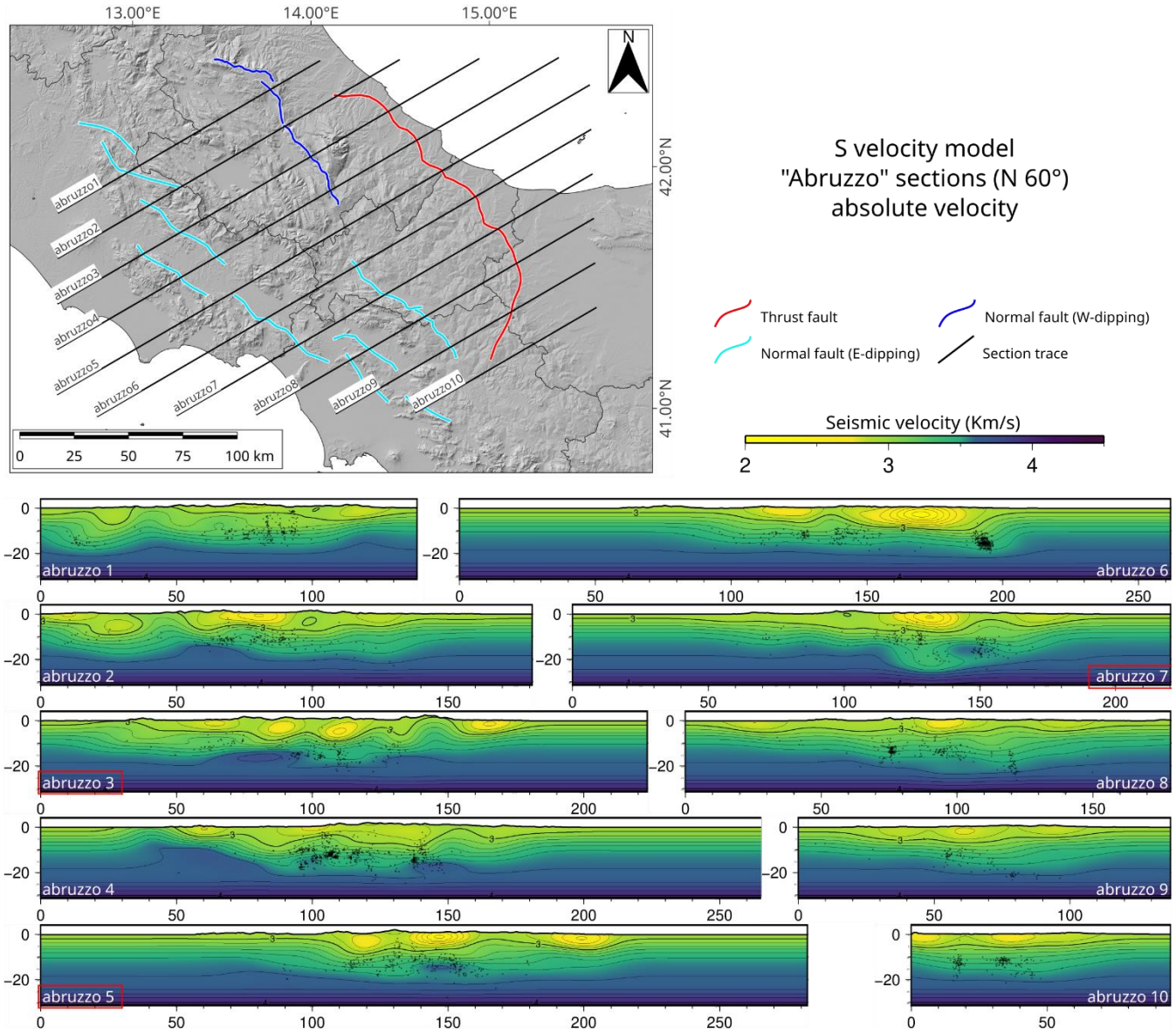

Figure S19. Vertical slices of the S tomographic model. Ten vertical cross-sections (abruzzo1-abruzzo10) spaced 9 km apart and oriented N60°E. The main contour lines are spaced at 1 km/s intervals, and the values are represented as absolute velocity. Red rectangle highlight the sections showing the velocity inversion.

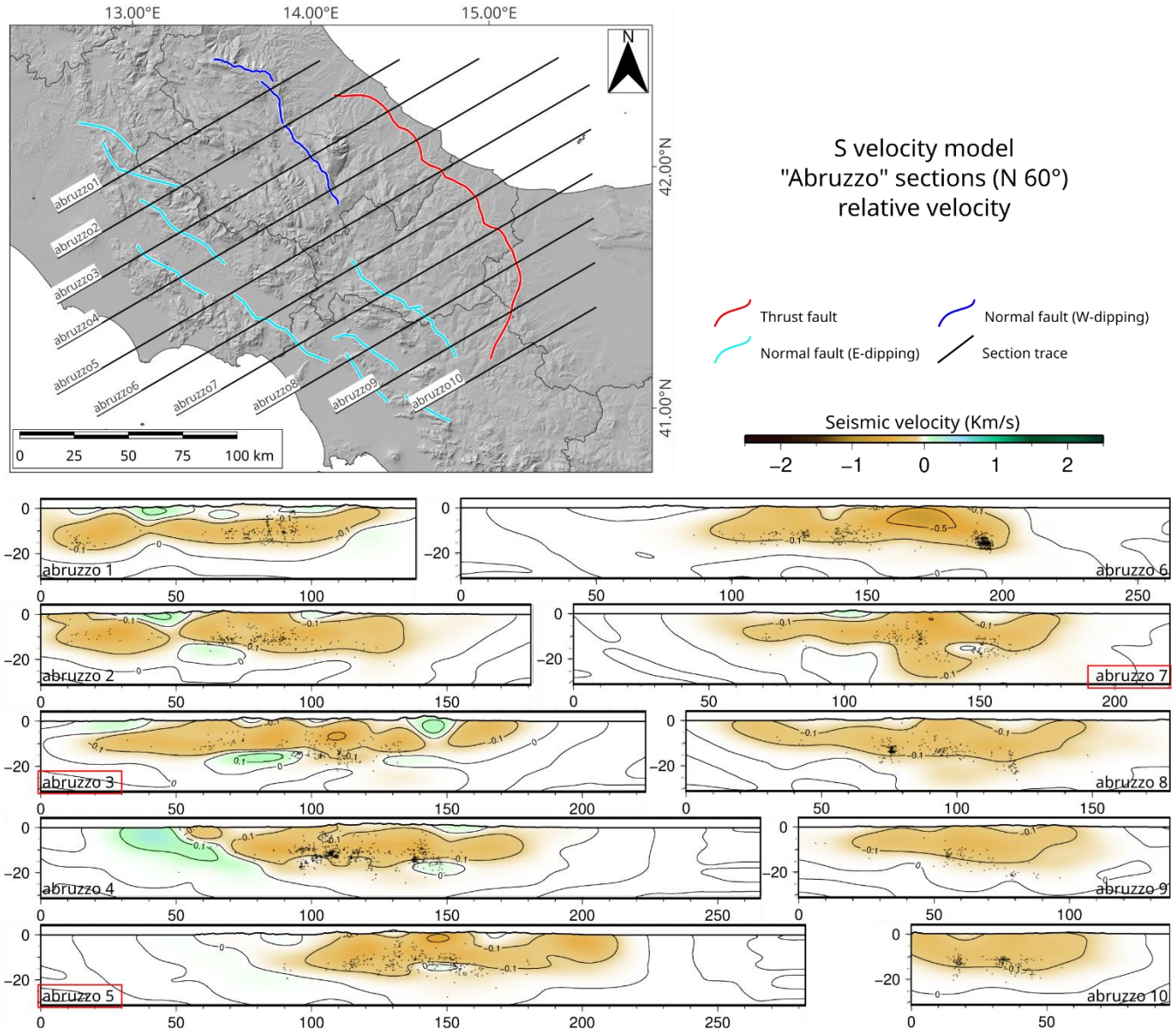

Figure S20. Vertical slices of the S tomographic model. Ten vertical cross-sections (abruzzo1-abruzzo10) spaced 9 km apart and oriented N60°E. The main contour lines are spaced at 1 km/s intervals, and the values are represented as relative velocity. Red rectangle highlight the sections showing the velocity inversion.

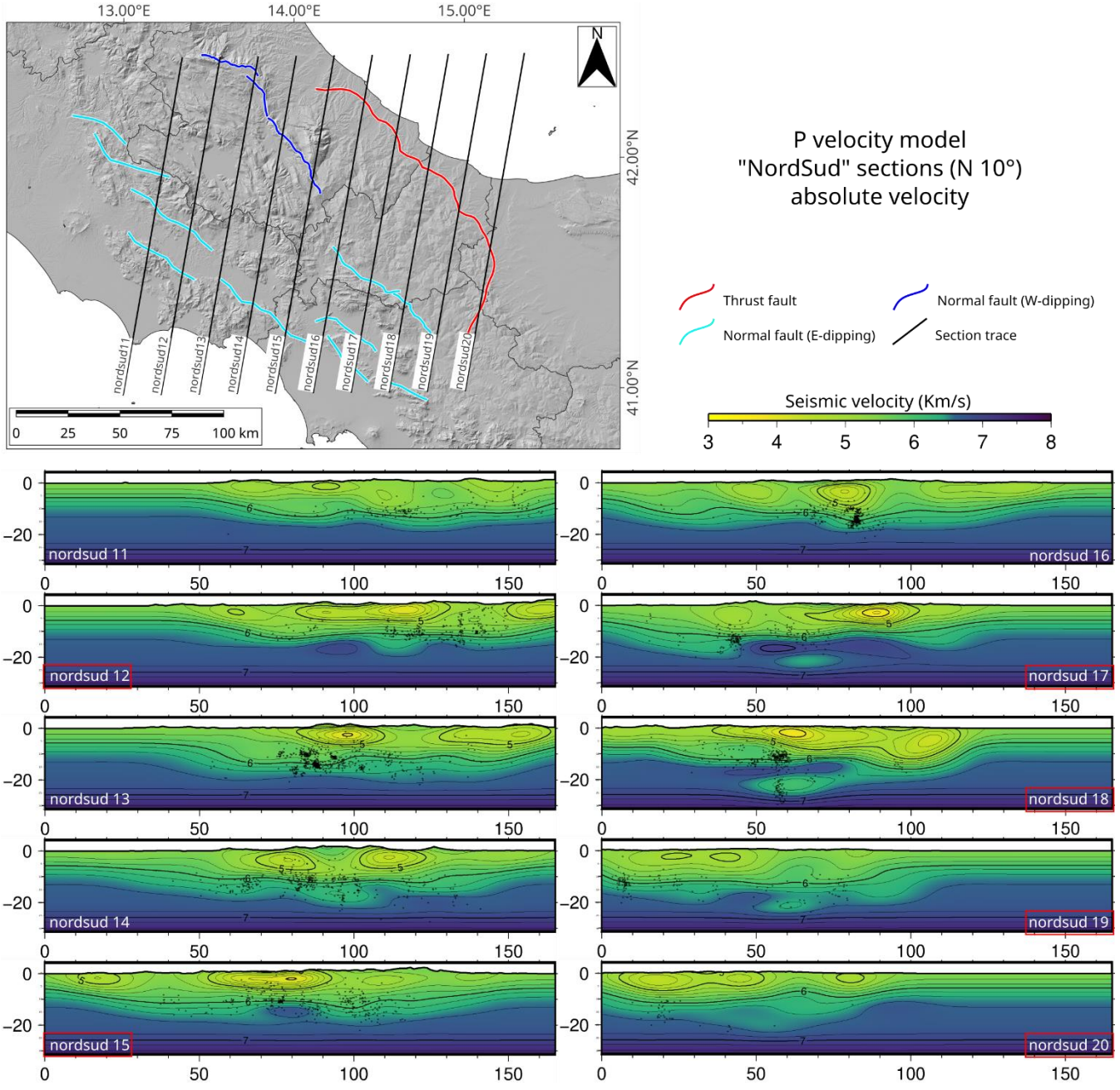

Figure S21. Vertical slices of the P tomographic model. Ten vertical cross-sections (nordsud11-nordsud20) spaced 9 km apart and oriented N10°E. The main contour lines are spaced at 1 km/s intervals, and the values are represented as absolute velocity. Red rectangle highlight the sections showing the velocity inversion.

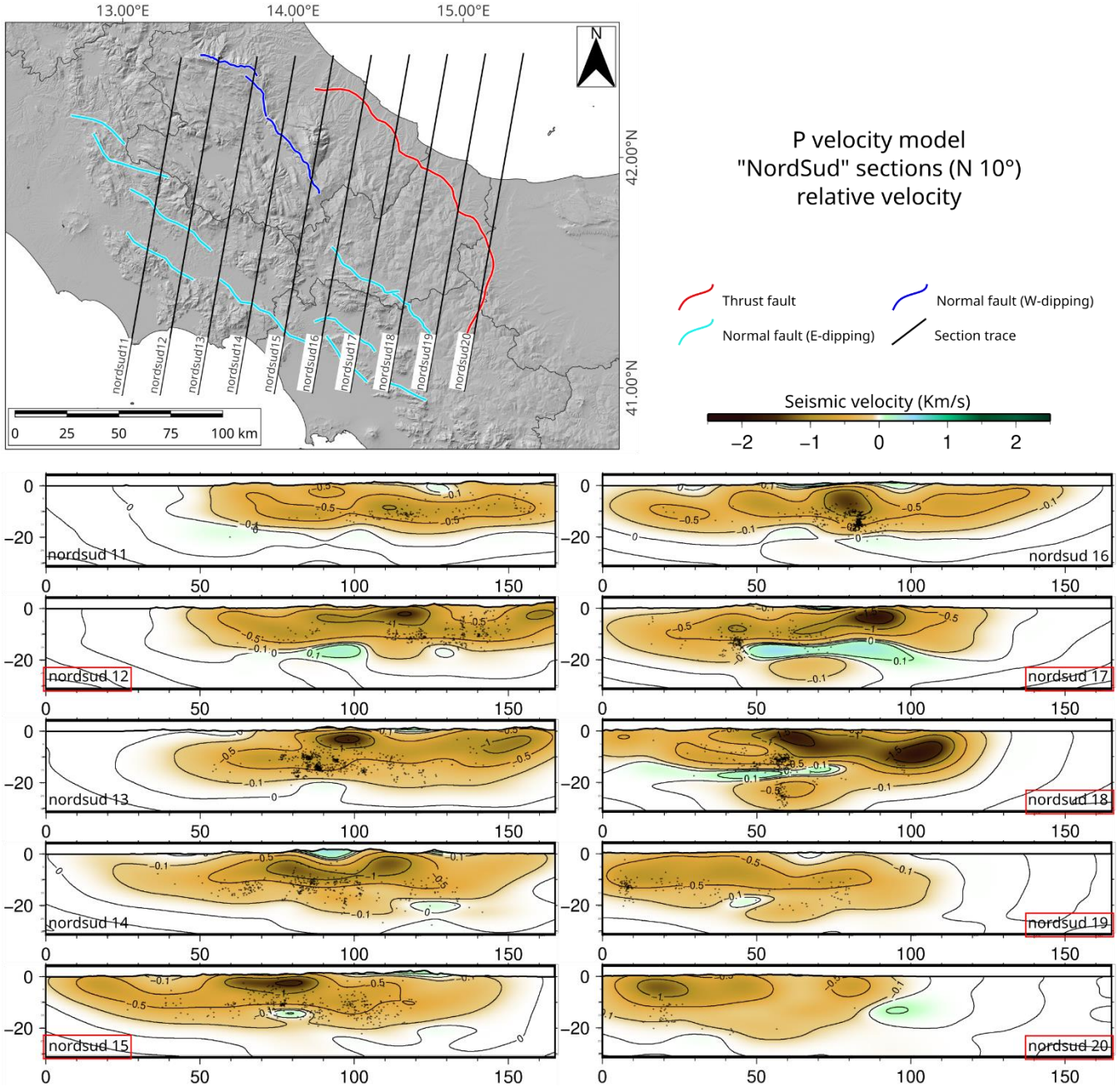

Figure S22. Vertical slices of the P tomographic model. Ten vertical cross-sections (nordsud11-nordsud20) spaced 9 km apart and oriented N10°E. The main contour lines are spaced at 1 km/s intervals, and the values are represented as relative velocity. Red rectangle highlight the sections showing the velocity inversion.

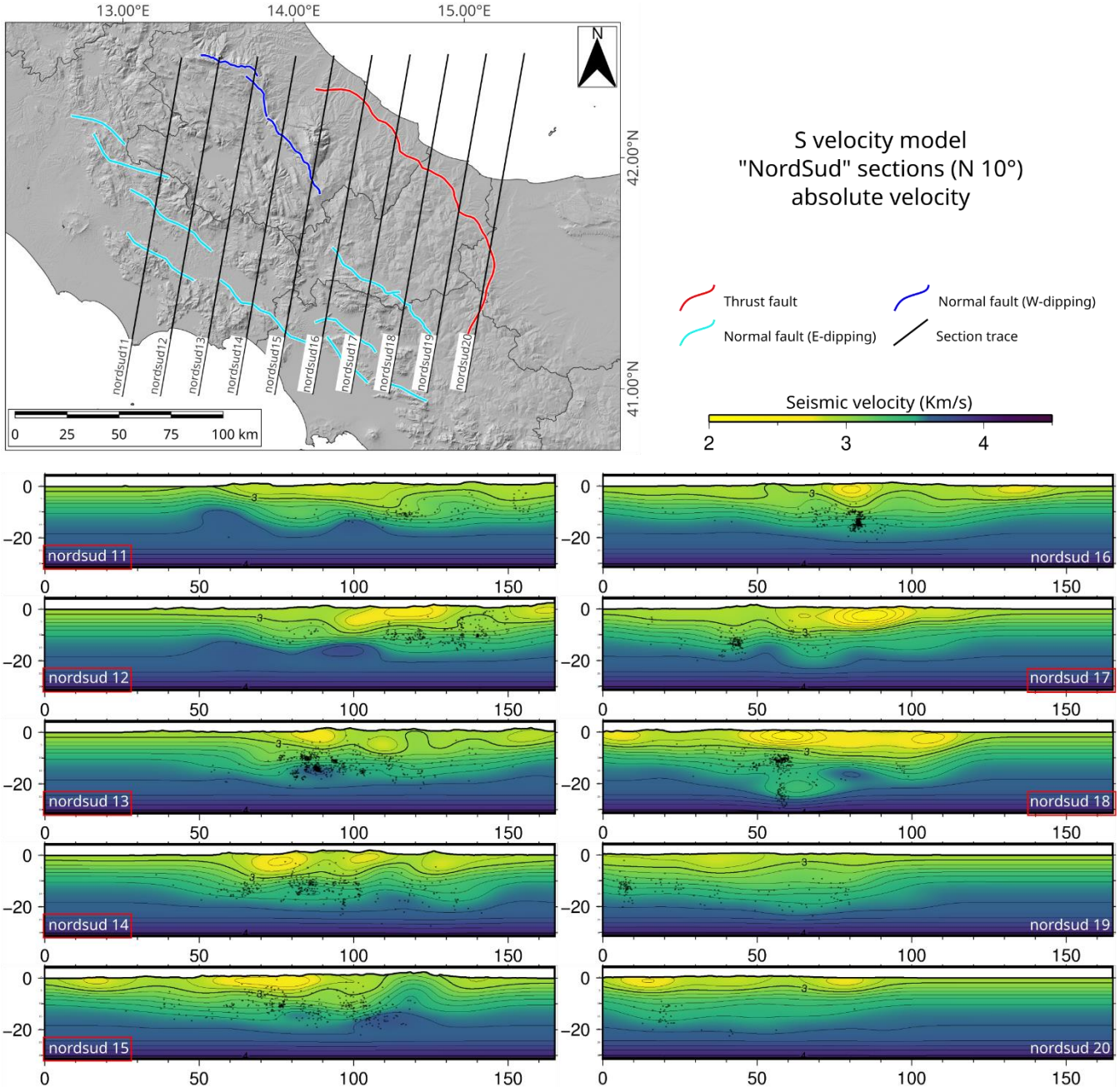

Figure S23. Vertical slices of the S tomographic model. Ten vertical cross-sections (nordsud11-nordsud20) spaced 9 km apart and oriented N10°E. The main contour lines are spaced at 1 km/s intervals, and the values are represented as absolute velocity. Red rectangle highlight the sections showing the velocity inversion.

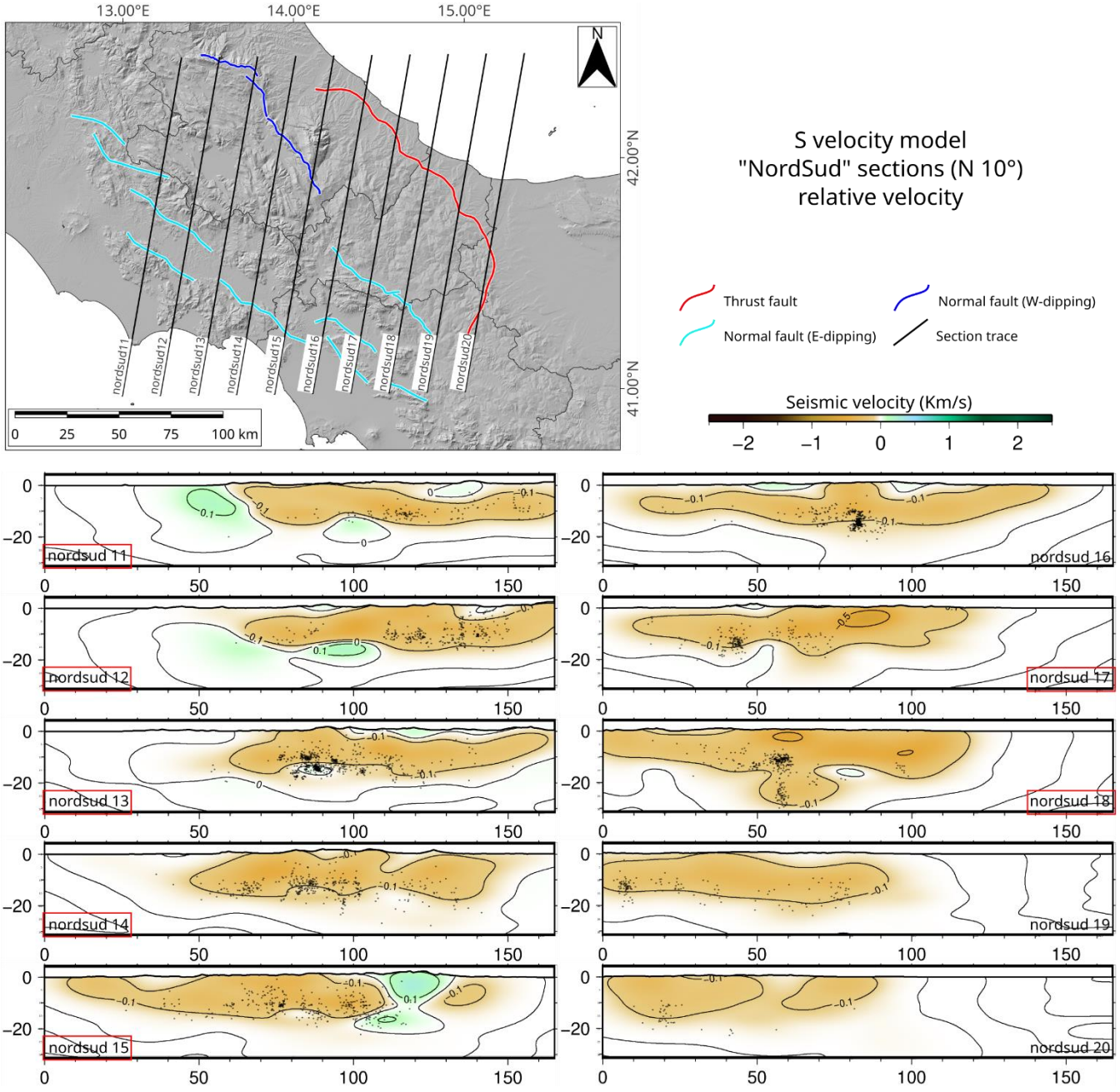

Figure S24. Vertical slices of the S tomographic model. Ten vertical cross-sections (nordsud11-nordsud20) spaced 9 km apart and oriented N10°E. The main contour lines are spaced at 1 km/s intervals, and the values are represented as relative velocity. Red rectangle highlight the sections showing the velocity inversion.

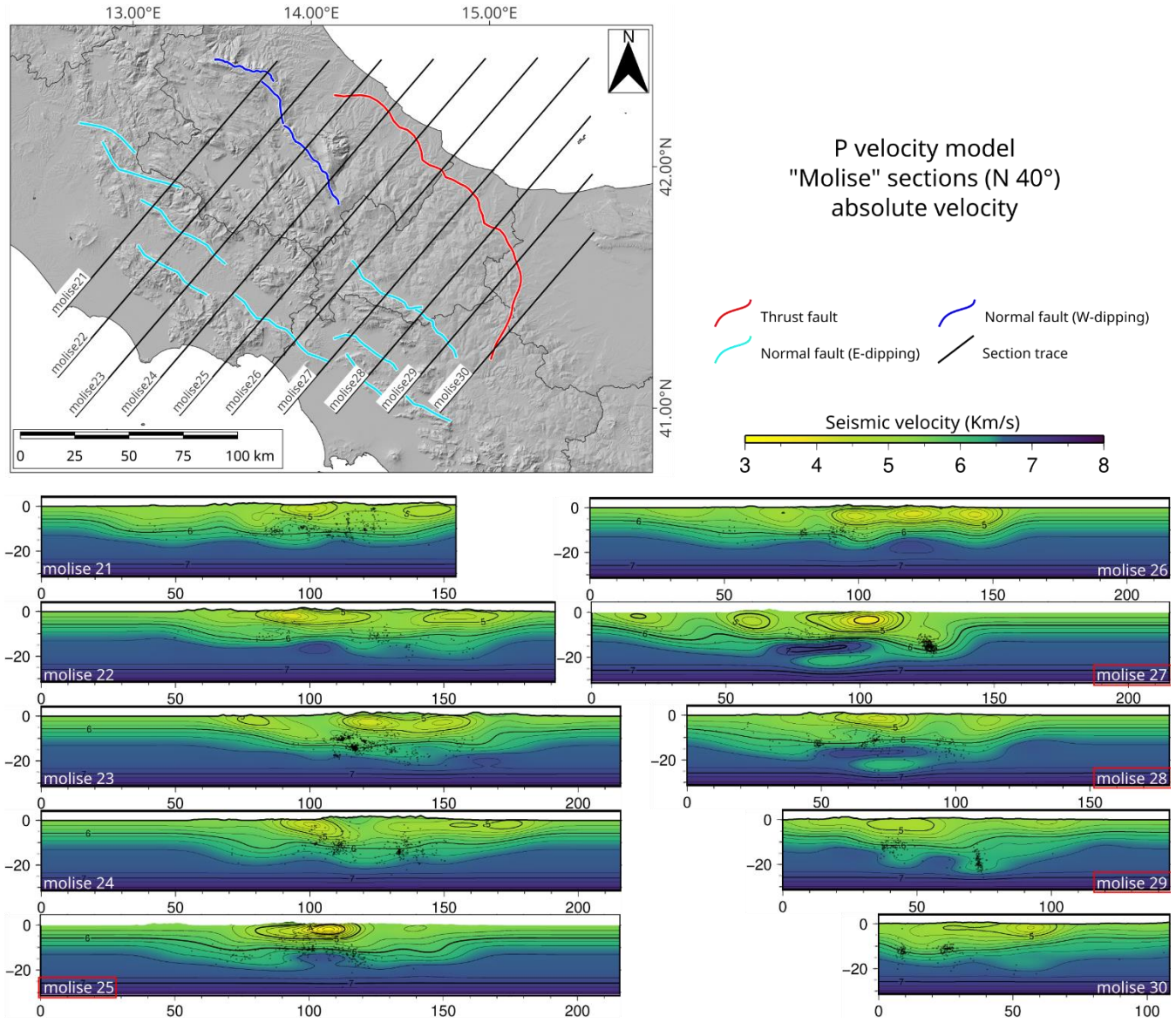

Figure S25. Vertical slices of the P tomographic model. Ten vertical cross-sections (molise21-molise30) spaced 9 km apart and oriented N40°E. The main contour lines are spaced at 1 km/s intervals, and the values are represented as absolute velocity. Red rectangle highlight the sections showing the velocity inversion.

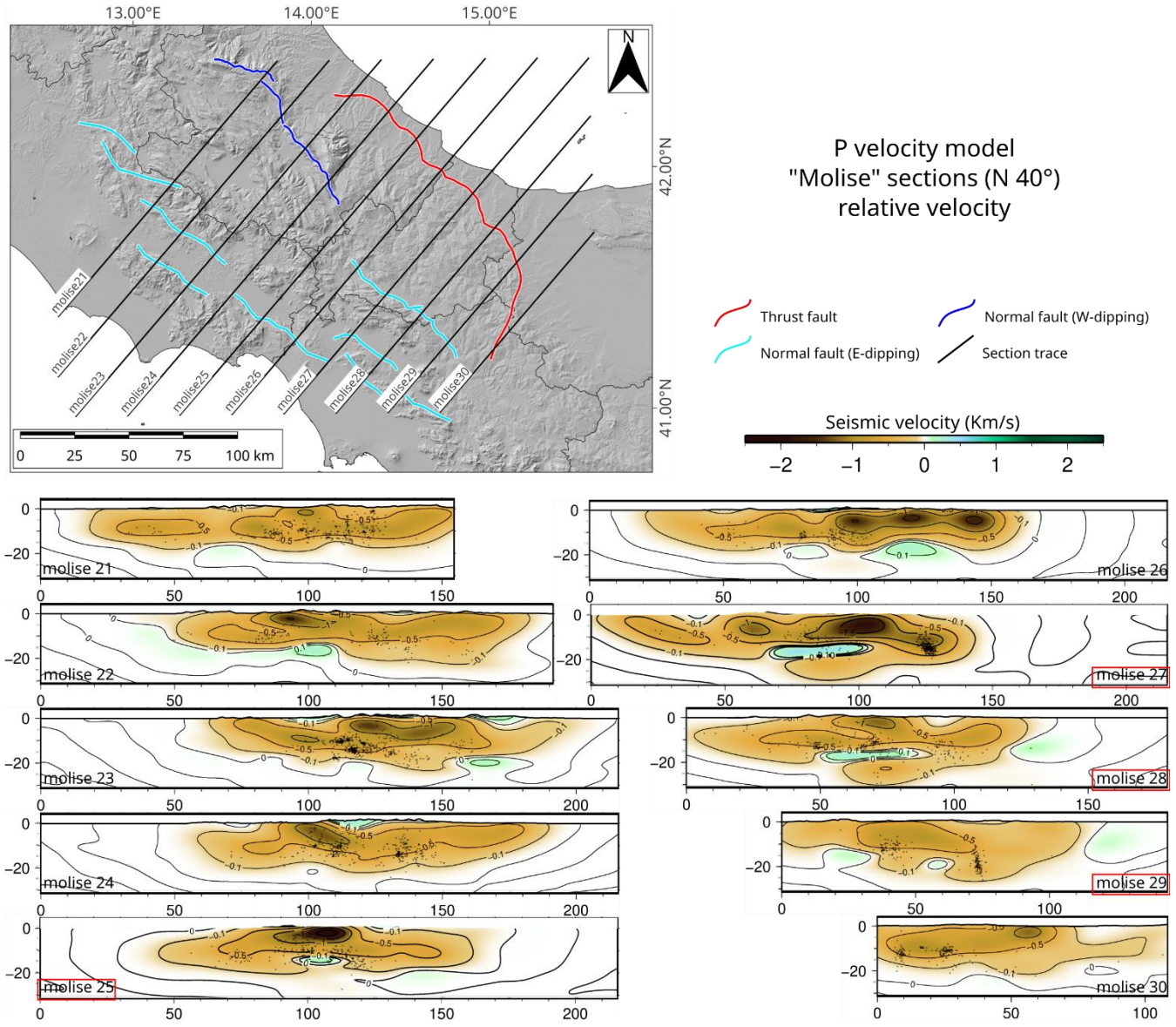

Figure S26. Vertical slices of the P tomographic model. Ten vertical cross-sections (molise21-molise30) spaced 9 km apart and oriented N40°E. The main contour lines are spaced at 1 km/s intervals, and the values are represented as relative velocity. Red rectangle highlight the sections showing the velocity inversion.

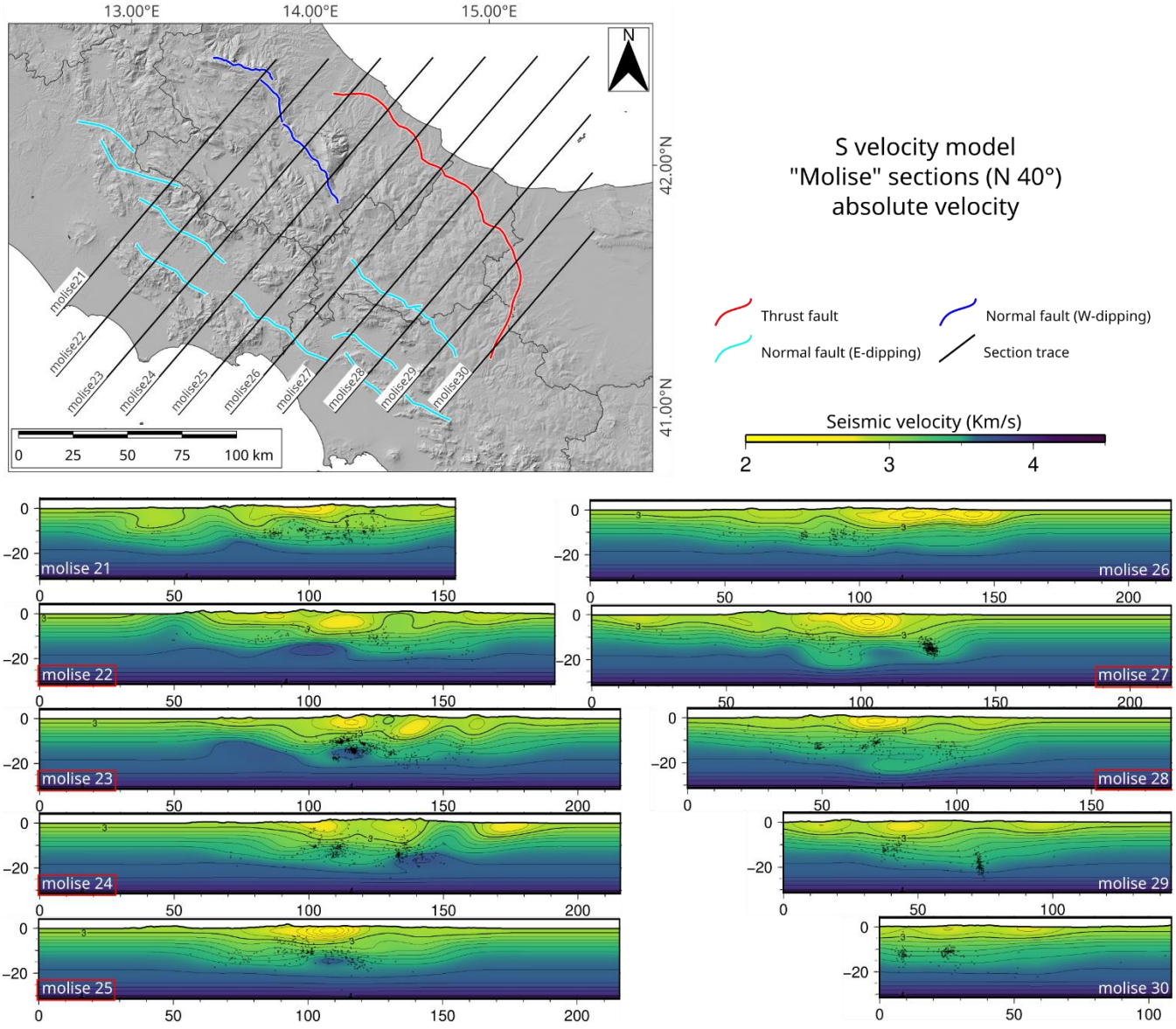

Figure S27. Vertical slices of the S tomographic model. Ten vertical cross-sections (molise21-molise30) spaced 9 km apart and oriented N40°E. The main contour lines are spaced at 1 km/s intervals, and the values are represented as absolute velocity. Red rectangle highlight the sections showing the velocity inversion.

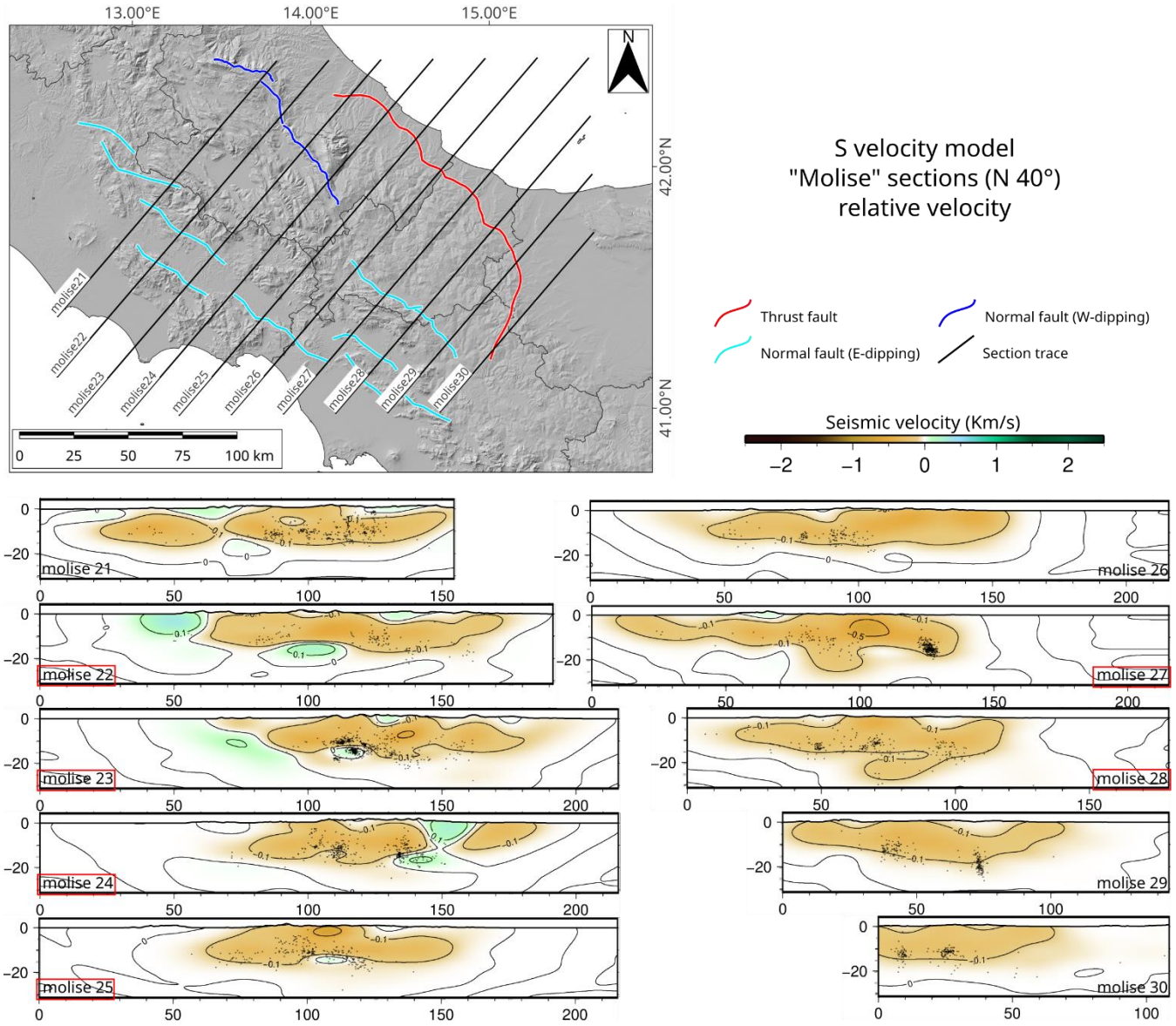

125 **Figure S28. Vertical slices of the S tomographic model. Ten vertical cross-sections (molise21-molise30) spaced 9 km apart and oriented N40°E. The main contour lines are spaced at 1 km/s intervals, and the values are represented as relative velocity. Red rectangle highlight the sections showing the velocity inversion.**

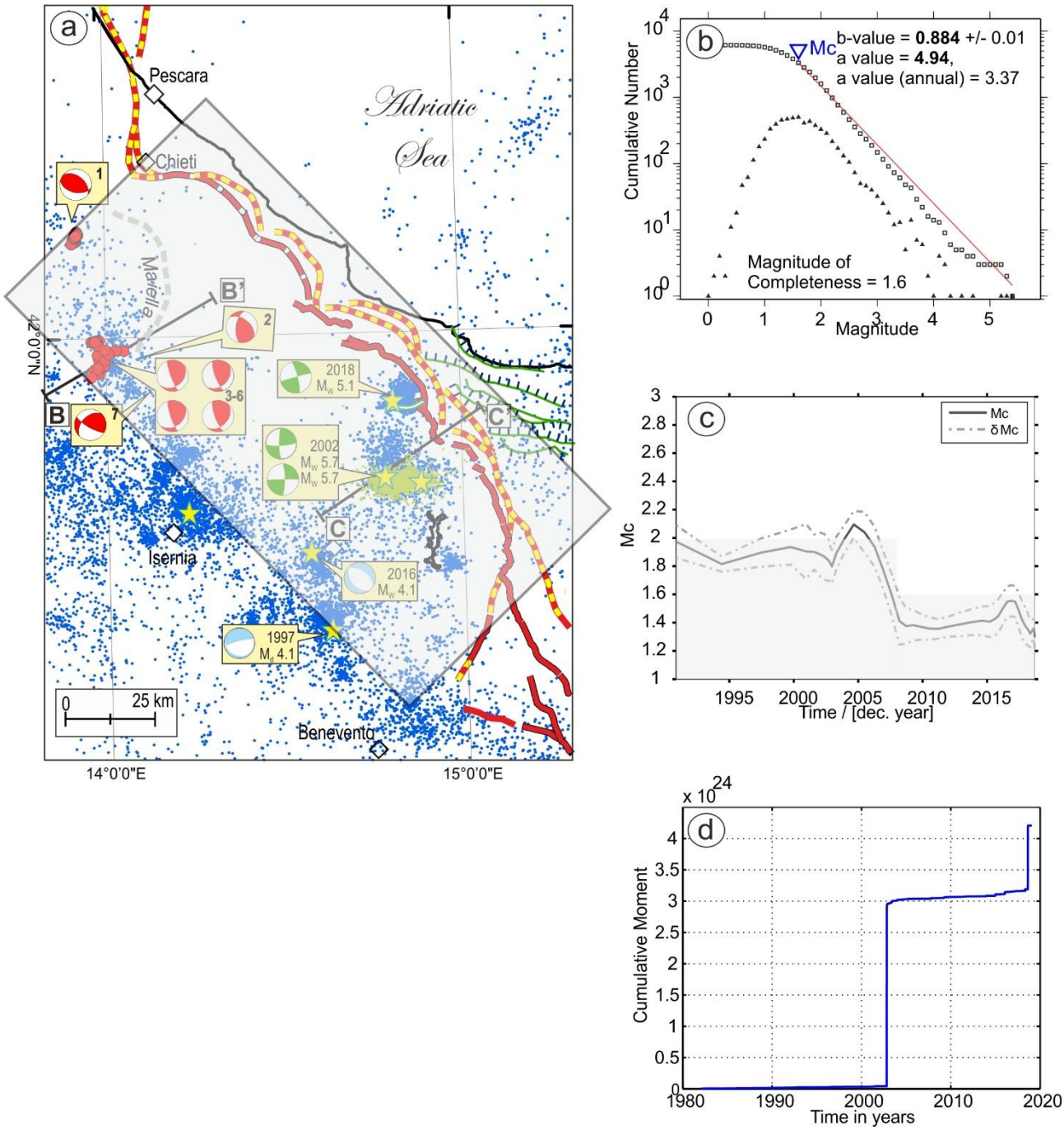

Figure S29. Analysis of the seismicity in the study area from 1981 to 2018 (Latorre et al., 2023). a) Location map. The rectangle encloses the seismic events considered in the analysis. b) Gutenberg–Richter slope evaluated with the events represented in panel a); blue triangle represents the completeness magnitude Mc. c) Completeness magnitude over time computed by the best combination of Mc95, Mc90, and Maximum Curvature (Woessner, 2005). Its uncertainty was evaluated with the bootstrap technique (Wiemer, 2000). d) Cumulative Moment over time.

Reference

Adinolfi, G. M., De Matteis, R., Orefice, A., Festa, G., Zollo, A., de Nardis, R., and Lavecchia, G.: The September 27, 2012, ML 4.1, Benevento earthquake: A case of strike-slip faulting in Southern Apennines (Italy), Tectonophysics, 660, 35–46, https://doi.org/10.1016/j.tecto.2015.06.036, 2015.

Bisio, L., Di Giovambattista, R., Milano, G., and Chiarabba, C.: Three-dimensional earthquake locations and upper crustal structure of the Sannio-Matese region (southern Italy), Tectonophysics, 385, 121–136, https://doi.org/10.1016/j.tecto.2004.01.007, 2004.

Butler, R. W. H., Mazzoli, S., Corrado, S., De Donatis, M., Di Bucci, D., Gambini, R., Naso, G., Nicolai, C., Scrocca, D., Shiner, P., and Zucconi, V.: Applying Thick-skinned Tectonic Models to the Apennine Thrust Belt of Italy — Limitations and Implications, in: Thrust Tectonics and Hydrocarbon Systems, American Association of Petroleum Geologists, 647–667, https://doi.org/10.1306/M82813C34, 2004.

Chiarabba, C., Bagh, S., Bianchi, I., De Gori, P., and Barchi, M.: Deep structural heterogeneities and the tectonic evolution of the Abruzzi region (Central Apennines, Italy) revealed by microseismicity, seismic tomography, and teleseismic receiver functions, Earth and Planetary Science Letters, 295, 462–476, https://doi.org/10.1016/j.epsl.2010.04.028, 2010.

Chiarabba, C., Buttinelli, M., Cattaneo, M., and De Gori, P.: Large Earthquakes Driven by Fluid Overpressure: The Apennines Normal Faulting System Case, Tectonics, 39, https://doi.org/10.1029/2019TC006014, 2020.

D'Ambrosio, A., Lipparini, L., Bigi, S., Cassola, T., Bambridge, V. R., Derks, J. F., and Trippetta, F.: Structural restoration and basin modelling of the central apennine orogen/foredeep/foreland system: New insights on the regional petroleum system, Marine and Petroleum Geology, 127, 104948, https://doi.org/10.1016/j.marpetgeo.2021.104948, 2021.

Ferrarini, F., Boncio, P., de Nardis, R., Pappone, G., Cesarano, M., Aucelli, P. P. C., and Lavecchia, G.: Segmentation pattern and structural complexities in seismogenic extensional settings: The North Matese Fault System (Central Italy), Journal of Structural Geology, 95, 93–112, https://doi.org/10.1016/j.jsg.2016.11.006, 2017.

Ferrarini, F., de Nardis, R., Brozzetti, F., Cirillo, D., Arrowsmith, J. R., and Lavecchia, G.: Multiple Lines of Evidence for a Potentially Seismogenic Fault Along the Central-Apennine (Italy) Active Extensional Belt–An Unexpected Outcome of the MW6.5 Norcia 2016 Earthquake, Front. Earth Sci., 9, 642243, https://doi.org/10.3389/feart.2021.642243, 2021.

Frepoli, A., Cimini, G. B., De Gori, P., De Luca, G., Marchetti, A., Monna, S., Montuori, C., and Pagliuca, N. M.: Seismic sequences and swarms in the Latium-Abruzzo-Molise Apennines (central Italy): New observations and analysis from a dense monitoring of the recent activity, Tectonophysics, 712–713, 312–329, https://doi.org/10.1016/j.tecto.2017.05.026, 2017.

Ghisetti, F. and Vezzani, L.: Normal faulting, transcrustal permeability and seismogenesis in the Apennines (Italy), Tectonophysics, 348, 155–168, https://doi.org/10.1016/S0040-1951(01)00254-2, 2002.

Improta, L., De Gori, P., and Chiarabba, C.: New insights into crustal structure, Cenozoic magmatism, CO_2 degassing, and seismogenesis in the southern Apennines and Irpinia region from local earthquake tomography: seismic tomography of Apennines, J. Geophys. Res. Solid Earth, 119, 8283–8311, https://doi.org/10.1002/2013JB010890, 2014.

Latorre, D., Di Stefano, R., Castello, B., Michele, M., and Chiaraluce, L.: An updated view of the Italian seismicity from probabilistic location in 3D velocity models: The 1981–2018 Italian catalog of absolute earthquake locations (CLASS), Tectonophysics, 846, 229664, https://doi.org/10.1016/j.tecto.2022.229664, 2023.

Mostardini, F. and Merlini, S.: Appennino Centro Meridionale - Sezioni Geologiche e Proposta di Modello Strutturale, Mem. Soc. Geol. It., 177–202, 1986.

Patacca, E., Scandone, P., Di Luzio, E., Cavinato, G. P., and Parotto, M.: Structural architecture of the central Apennines: Interpretation of the CROP 11 seismic profile from the Adriatic coast to the orographic divide: CROP 11 SEISMIC PROFILE, Tectonics, 27, n/a-n/a, https://doi.org/10.1029/2005TC001917, 2008.

Romano, M. A., De Nardis, R., Garbin, M., Peruzza, L., Priolo, E., Lavecchia, G., and Romanelli, M.: Temporary seismic monitoring of the Sulmona area (Abruzzo, Italy): a quality study of microearthquake locations, Nat. Hazards Earth Syst. Sci., 13, 2727–2744, https://doi.org/10.5194/nhess-13-2727-2013, 2013.

Rovida, A., Locati, M., Camassi, R., Lolli, B., and Gasperini, P.: The Italian earthquake catalogue CPTI15, Bulletin of Earthquake Engineering, 18, 2953–2984, https://doi.org/10.1007/s10518-020-00818-y, 2020.

Rovida, A., Locati, M., Camassi, R., Lolli, B., Gasperini, P., and Antonucci, A.: Catalogo Parametrico dei Terremoti Italiani (CPTI15), versione 4.0 (4.0), https://doi.org/10.13127/CPTI/CPTI15.4, 2022.

Scafidi, D., Solarino, S., and Eva, C.: P wave seismic velocity and Vp/Vs ratio beneath the Italian peninsula from local earthquake tomography, Tectonophysics, 465, 1–23, https://doi.org/10.1016/j.tecto.2008.07.013, 2009.

Speranza, F. and Chiappini, M.: Thick-skinned tectonics in the external Apennines, Italy: New evidence from magnetic anomaly analysis: THICK-SKINNED TECTONICS IN THE APENNINES, J. Geophys. Res., 107, ETG 8-1-ETG 8-19, https://doi.org/10.1029/2000JB000027, 2002.

Trionfera, B., Frepoli, A., De Luca, G., De Gori, P., and Doglioni, C.: The 2013–2018 Matese and Beneventano Seismic Sequences (Central–Southern Apennines): New Constraints on the Hypocentral Depth Determination, Geosciences, 10, 17, https://doi.org/10.3390/geosciences10010017, 2019.

Vezzani, L., Festa, A., and Ghisetti, F. C.: Geology and Tectonic Evolution of the Central-Southern Apennines, Italy, in: Geology and Tectonic Evolution of the Central-Southern Apennines, Italy, Geological Society of America, https://doi.org/10.1130/2010.2469, 2010.

Wiemer, S.: Minimum Magnitude of Completeness in Earthquake Catalogs: Examples from Alaska, the Western United States, and Japan, Bulletin of the Seismological Society of America, 90, 859–869, https://doi.org/10.1785/0119990114, 2000.

Woessner, J.: Assessing the Quality of Earthquake Catalogues: Estimating the Magnitude of Completeness and Its Uncertainty, Bulletin of the Seismological Society of America, 95, 684–698, https://doi.org/10.1785/0120040007, 2005.